A Statistical study of large amplitude parallel electric fields in the upward current region of the auroral acceleration region

A. J. Hull, J. W. Bonnell and F. S. Mozer
Space Sciences Laboratory, University of California, Berkeley

J. D. Scudder
Department of Physics and Astronomy, University of Iowa, Iowa City

HULL ET AL.: PARALLEL ELECTRIC FIELDS

Abstract. We present a survey of 64 direct observations of large amplitude parallel electric fields $E_{||}$ in the upward current region of the southern auroral acceleration zone obtained by the three-axis electric field experiment on Polar. These $E_{||}$ events range in amplitude from about 25 mV/m to 300 mV/m and represent a significant fraction of the total electric field strength ($E_{||}/E_{\perp}$ ranges from ~ 0.25 to O(1)). The $E_{||}$ structures, which tend to occur at the edges of oppositely directed (converging) pairs of perpendicular electric field structures (electrostatic shocks), have transverse (to the magnetic field) widths of $\sim 1.0 - 20$ km at altitudes ranging from 0.8 to 1.5 R_{E}, assuming the structures are stationary. The parallel potential drops associated with these large amplitude parallel electric fields are highly localized in altitude (e.g., tens of kilometers as opposed to $\sim 10^3$ km). The occurrence of these events falls of dramatically with altitude. The amplitude of the parallel electric field shows a strong anticorrelation with the plasma density inferred from spacecraft potential measurements. We find no apparent correlation between the amplitude of the parallel electric field and altitudes sampled (between 0.8 and 1.5 R_{E}), current, and K_p, though there is a suggestion that the largest $E_{||}/E_{\perp}$ ratios are confined to lower altitudes. A detailed analysis seems to favor ambipolar effects over electron inertial effects as an explanation for the parallel electric field signatures.

1. Introduction

Electric fields parallel to the magnetic field vector play a major role in the transport of mass, momentum, and energy in the auroral zone. In the upward current region, higher altitude, large amplitude perpendicular electric fields $E_\perp$ are prevented from mapping to the ionosphere via a parallel electric field $E_{||}$. The $E_{||}$ is of a sense to accelerate ions of ionospheric origin upwards and magnetospheric electrons downward, maintaining current and quasineutrality in the presence of a mirroring magnetic field. The parallel potential drop experienced by the particles typically ranges from 1 to 10 kV. Although localized in latitude, the parallel potential is usually envisioned to be distributed over a large altitude extent ($\sim$ thousands of kilometers), giving rise to a relatively small amplitude $E_{||}$ ($\sim$ few mV/m) throughout the acceleration region. The generally accepted model of the canonical U-shaped potential well is depicted in Figure 1a, as a reference. **Figure 1.**

Large amplitude, macroscopic parallel electric fields were first encountered by S3-3 [e.g., *Mozer et al.*, 1980] and more recently by Polar [*Mozer and Kletzing*, 1998; *Mozer and Hull*, 2001]. The few examples from Polar had amplitudes ranging from 200-300 mV/m and occurred in the southern auroral acceleration region at altitudes of about 6400 km on the boundary between high and low density plasma. Such large amplitude parallel electric fields imply significant parallel potential drops distributed over tens of kilometers, as opposed to potential drops distributed over thousands of kilometers. *Mozer and Hull* [2001] suggested that the large parallel electric fields are part of the field structure of the auroral acceleration region and they occur in a "sheath" that separates the dense ionosphere from the less dense, higher altitude region. Figure 1b illustrates a revised U-shaped model of the potential well envisioned by *Mozer and Hull* [2001]. Thus, in addition to weak parallel electric fields that exist at mid to high altitudes, the auroral acceleration region is envisioned to have large parallel electric fields at low altitudes. Highly localized, large amplitude parallel electric fields have also been suggested in recent simulations [*Ergun et al.*, 2000], as can be inferred from sharp transitions separating distinct regions of the modeled acceleration region. *Ergun et al.* [2000] found that the occurrence of the sharp transitions in potential was sensitive to the boundary conditions imposed.

It is not obvious whether localized parallel electric fields are a property of the typical state of the auroral acceleration region or arise under special circumstances. Statistical studies of direct measurements of parallel electric fields as a function of longitude, latitude, and altitude are essential to understanding the morphology of the parallel potential, the mechanism or mechanisms responsible their formation, and their relation to particle acceleration. To date only a few examples of large amplitude parallel electric fields exist in the literature. In this study we present a statistical survey of 64 large amplitude $E_{||}$ structures measured in the southern auroral acceleration region by the three-axis electric field experiment on Polar at altitudes from 0.8 R_{E} to 1.5 R_{E}. The $E_{||}$ events have peak amplitudes ranging from 25 mV/m to 300 mV/m and represent a significant fraction of the total electric field strength ($E_{||}/E_{\perp}$ range from $\sim$ 0.25 to O(1)). In section 3 we present a few case studies of $E_{||}$ to illustrate some of their characteristic properties. Section 4 establishes the statistical properties of the $E_{||}$ structures in relation to other parameters that characterize the auroral acceleration region. In section 5 we test the degree to which the large amplitude parallel electric fields can be explained by electron inertia and ambipolar effects. The ambipolar term of the generalized Ohm's law is found to be a plausible explanation for these large amplitude macroscopic parallel electric field signatures discussed in this paper, while the electron inertial term is not. Conclusions are given in Section 6.

2. Instrumentation and Experimental Data Set

The electric field data used in this study were measured by the electric field instrument (EFI) on board Polar [*Harvey et al.*, 1995]. EFI consists of three orthogonal sphere pairs that measure the electric field vector. The spin plane double probes have separations of 100 and 130 m, respectively. The third pair of spheres lie along the spin axis and are held 14 m apart by rigid booms. The electric field is regularly sampled at a rate of 40 vectors per second through a 20 Hz low-pass filter. Magnetic field data at 8 vectors per second were provided by the Polar magnetic field experiment (MFE) [*Russell et al.*, 1995]. Burst electric field data, sampled at 1600 Hz, were available for one of the events discussed in the paper. The burst electric field signals were low-pass filtered at 500 Hz. The search coil magnetic fields [*Gurnett et al.*, 1995] were sampled at the same rate as the burst electric field data.

The electric field data used in this study are presented in a local magnetic field aligned coordinate (FAC) system in which the z-axis represents the direction along the magnetic field, the x-axis is in the magnetic meridional plane and points equatorward, and the y-axis completes the orthonormal set and points in the magnetic westward direction. Spin period averaged magnetic field data were used to determine the local magnetic field aligned coordinate system.

The high time resolution (1.15s) electron and ion data used in this paper were measured by the DuoDeca Electron Ion Spectrometer (DDEIS) component of the HYDRA instrument onboard Polar [*Scudder et al.*, 1995]. The DDEIS is composed of 6 pairs of E/Q analyzers which measure counts in 12 look directions with narrow fields of view ($8^\circ \times 8^\circ$) and energy bandwidth of $\Delta E/E = 6\%$, alternating between electron and ion samples in subsequent energy sweeps (1.15 s). Each sweep consists of 16 logarithmic energy steps from about 12 eV to 18 keV. Unless specifically stated otherwise, the electron and ion data used in this study have been corrected for spacecraft floating potential using direct measurements from EFI.

In this study the following criteria were used to select candidate parallel electric field events: (1) $E_{||}$ candidates must not be affected by the spin axis measurement. The spin axis measurements are less reliable than the spin plane measurements because the spin axis booms are much shorter than the spin plane booms and DC offsets associated with asymmetries in the spin axis booms are difficult to determine. (2) $E_{||}$ must have a significant amplitude (e.g. $E_{||} \gtrsim 25$ mV/m). This criteria filters out those events that can be caused by uncertainties in the spin-plane offset determination. Events found to be sensitive to offset corrections were excluded from the database. (3) We require that the $E_{||}$ signal must not be significantly affected by arbitrary rotations of $\pm 5°$ of the magnetic field. A number of events are associated with large amplitude perpendicular electric fields. False $E_{||}$ events could result from the projection of $E_{\perp}$ along the field line via errors in the magnetic field direction and errors in the coordinate transformations from the S/C frame to the FAC system. (4) Large fields must not saturate the probe electronics. Sufficiently large electric fields may saturate the probes and cause unphysical $E_{||}$ signals. Events contaminated by probe saturation were identified and removed from this data set. (5) "Shadow" effects must be small. As a result of the different manners in which the net current to each probe gets balanced, a voltage difference between a pair of spherical probes can be induced when one of the detectors is solar illuminated and the other is in shadow. The spurious spin periodic signal is relatively easy to identify, showing up when the spin plane boom axis is aligned with the sun-S/C direction. (6) Orthogonal estimates of the spacecraft potential must agree. This criteria effectively filters out spurious fields attributed to wake effects and high ambient density problems (e.g. when one of the probes lies in an undesirable part of the Langmuir characteristic). (7) A complementary criteria to (6) is that all of the probes must respond to the electric field in the event.

3. Case studies of $E_{||}$

Three years of Polar EFI data from April 1996 to February 1998 yielded 64 events that satisfied our selection criteria. In this section, we provide a few examples of large amplitude, macroscopic $E_{||}$ structures encountered by Polar in the southern auroral zone. The events chosen are representative of the $E_{||}$ structures that make up our statistical database. We give evidence suggesting that the macroscopic parallel electric field structures, which are the focus of this paper, are different from the short duration, large amplitude solitary structures previously reported in the literature [e.g., *Temerin et al.*, 1982; *Cattell et al.*, 1999] or ion cyclotron wave fields with significant electric field component along the magnetic field vector. Moreover, we tested the kinetic Alfvén wave expectation of the parallel and perpendicular fields and demonstrated that at least for the example tested the Alfvén explanation does not appear to be feasible.

3.1. September 14, 1996 event

Plate 1.

An example of a southern auroral zone crossing on September 14, 1996 at an altitude of $\sim 1R_{\mathrm{E}}$ is illustrated in Plate 1. The three hour averaged K_p was 2+. Polar was near local noon at an invariant magnetic latitude $\sim 75°$, and with increasing time it moved poleward (toward higher invariant latitude) across a region of small amplitude electric fields to subsequently encounter a region containing large amplitude electric field structures occurring after about 0622:10 UT (see Plates 1a-1c). Plates 1a-1c depict the 3 components of the electric field in the field aligned coordinate system defined earlier. It is important to note that the y-axis range for Plate 1c is different from that of Plates 1a and 1c to make the parallel electric field component clearly visible. In Plate 1c, parallel electric fields ranging in amplitude from 70 mV/m to 35 mV/m are observed near 0622:13 UT and 0622:26 UT, respectively. The $E_{||}$ events appear to occur between opposing (converging) pairs of large amplitude perpendicular electric fields (see Plates 1a and 1b), which range in amplitude from 200 mV/m to 350 mV/m. The peak $E_{||}/E_{\perp}$ ratio for these events are found to be 15 and 10, respectively. Plate 1d depicts the negative of the spacecraft floating potential Φ_{SC}, which is a proxy for the plasma density. Values of Φ_{SC} near zero correspond to high density plasma, whereas large negative values of Φ_{SC} correspond to low density plasma. In this example the density ranges from ~ 10 cm^{-3} in the low field regions to a minimum of ~ 0.1 cm^{-3} in the regions that correspond to large amplitude electric field signatures. The east-west component of the magnetic field perturbation ΔB_Y is given in Plate 1e. The slope provides an estimate of the amplitude of the field aligned current. The decrease in ΔB_Y with increasing invariant magnetic latitude during the interval encompassing the $E_{||}$ events ($\sim$ 0622:10 UT to 0622:50 UT) suggests that $E_{||}$ occurred in a region of upward field aligned current. Plate 1f shows the plasma potential $\Phi_{\rm pl}$, which is determined by integrating $E_{\perp}$ along Polar's trajectory. The parameter $\Phi_{\rm pl}$ is a measure of potential below Polar assuming a quasistatic potential model. Plate 1f suggests a ~ 1 kV parallel potential drop below the spacecraft during the $E_{||}$ intervals.

Spectrograms of ion differential energy flux for pitch angle ranges from 150°-180° (downward) and 0°-30° (upward) are depicted in Plates 1g and 1h, respectively. Similarly, electron spectrograms for pitch angle ranges from 150°-180° and 0°-30° (upward) are depicted in Plates 1i and 1j, respectively. Plates 1k and 1l display spectrograms of the ion and electron skew defined as the difference between the field-aligned and opposed differential energy fluxes normalized by the estimated systematic and statistical measurement uncertainty in that difference. Intense field-aligned ion beams with a mean energy of ~ 1 keV are shown to be concurrent with the large amplitude parallel electric fields (see Plates 1g and 1h). The variation of ion beam energy is shown to be consistent with the variation of $\Phi_{\rm pl}$ depicted in the Plate 1f. The predominance of the upgoing ion flux with respect to the downgoing flux is apparent from the yellow to orange enhancements in the ion skew displayed in Plate 1k from about 0622:10 to 0622:30 UT. Enhancements in the downgoing electron energy flux are observed simultaneously with the upgoing ion beams (Plate 1j). The blue in electron skew depicted in Plate 1l from 0622:10 to 0622:30 UT associated with the downward electron enhancements seen in Plate 1j indicates predominantly downward electron fluxes. **Plate 2.**

One-second resolution electron and ion velocity space distribution functions near

0622:26 are illustrated in Plates 2a and 2b, respectively. In the southern auroral zone positive (negative) values of $v_{||}$ are associated with particles moving away from (towards) Earth. Corresponding one-second resolution cuts of the electron and ion distribution function aligned (red curve), opposed (blue curve), and perpendicular (magenta curve) to the magnetic field vector $\hat{\mathbf{b}}$ are exhibited in Plates 2c and 2d, respectively. The solid black curve represents the energy spectrum averaged over all pitch-angles. The spectra depicted in Plates 2c and 2d have not been corrected for the spacecraft floating potential. The dotted vertical line indicates the spacecraft potential. The dotted diagonal line represents the average one-count level of the 1.15 s sampling interval. The spectra are averaged over a finite pitch-angle extent of roughly 30°. Some of the bins used to get the average spectra have no counts, thus at times the spectra may fall below the average one count level. The downward cut (blue curve) of the electron distribution function in Plate 2c is basically flat with a phase space density that is an order of magnitude larger than the upward cut (red curve). This is characteristic of a modified loss-cone distribution of electrons which results from the interaction of magnetized electrons with the parallel potential and mirroring magnetic field. In going from the plasmasheet to the ionosphere, a fraction of the electrons get mirrored. However, a parallel electric field exists and accelerates enough electrons through the magnetic mirror, so as to guarantee quasineutrality and maintain current balance. The flat part of the distribution function is often interpreted as the end state of an accelerated electron beam after quasi-linear plateau formation.

A rough estimate of the vertical extent of the parallel electric field can be obtained by assuming that the macroscopic parallel electric field is responsible for all of the electron acceleration and is uniformly distributed in altitude. Such an approximation is motivated by the recent simulations by *Ergun et al.* [2000], which suggested the existence of significant parallel potential drops concentrated in very thin layers ($\lesssim$ 125 km). The downward pointing edge of the parallel cut of the electron flat-top distribution function provides a rough measure of the potential seen by the electrons above the spacecraft. Using the respective observed values of 35 mV/m and 1 keV for the parallel electric field amplitude and the parallel potential, the vertical extent of the potential above the spacecraft is estimated to be $\approx$ 30 km. The ion distribution is a beam, which suggests a net parallel potential of $\sim$1 keV and hence an estimated 30 km vertical extent below the spacecraft.

Our estimates of the altitudinal extent of the parallel potential suggest that if all or most of the parallel potential drop seen by the particles is due to the large amplitude parallel electric field, then the auroral acceleration region must be confined to a narrow region roughly tens of kilometers in extent, as opposed to thousands of kilometers. However, previous observations [*Mozer and Hull*, 2001] suggest via observations of inverted-V electrons at higher altitudes (2 to 5 R_{E}) the existence of weak parallel electric fields. Thus it is likely that these large amplitude parallel electric fields observed at low altitudes are accompanied by weaker parallel electric fields at higher altitudes. What is not obvious is whether most of the parallel potential drop seen by the particles is due to the large amplitude parallel electric field at low-altitudes, the weak parallel electric fields at higher altitudes, or if significant contributions come from both. Accordingly, our estimates represent an upper limit of the vertical extent of the parallel potential drop associated with the large amplitude parallel electric fields.

The presence of both upward accelerated ions and downward precipitating electrons suggests that Polar is traversing the upward current portion of the auroral acceleration proper. A model of the equipotential configuration along the field line consistent with the observations is given in Figure 1c. The auroral zone proper is envisaged to be composed of a pair of U-shaped, elongated structures with intense parallel electric fields occurring in a highly localized region (tens of kilometers) near the bottom of the potential tongues, and weak parallel electric fields at higher altitudes. This scenario is to be contrasted with the generally accepted paradigm of the equipotential morphology, which is viewed to be U-shaped, with a parallel potential distributed over thousands of kilometers as depicted in Figure 1a. The large $E_{||}/E_{\perp}$ ratios that characterize the $E_{||}$ events suggest boundary crossings with respective normals inclined at angles of 4° and 6° with respect to magnetic field. Thus, we view Polar to be traversing the bottom edge of the potential tongues within the region of concentrated parallel potential due to a large amplitude parallel electric field, as indicated by the dashed arrow.

3.2. May 30, 1998 event

Figure 2.

Macroscopic parallel electric fields with significant amplitude were observed by Polar on May 30, 1998, at an altitude of about 5400 km. Polar was near midnight at an invariant magnetic latitude of $\sim 67°$, and was moving poleward. The K_p index for these events was 4. The region is characterized by an upward field aligned current with an amplitude of roughly 0.3 μA/m^2 estimated from the slope (gradient) of the magnetic field perturbation (data not shown). Figures 2(a)–2(c) depict time series of the 40-Hz sampled electric field data in the FAC system. Large scale $E_{||}$ occur in two intervals ($\sim$ 0324:33.2 – 0324:33.7 UT and $\sim$ 0324:34.0 – 0324:34.8 UT, respectively) with significant peak amplitudes ranging from 65 mV/m to roughly 100 mV/m (see Figure 2(c)). The $E_{||}$ structures are nearly coincident with large amplitude $E_{\perp}$ structures shown in Figure 2(a) and have a sense such that $\mathbf{J} \cdot \mathbf{E} > 0$. The peak $E_{||}/E_{\perp}$ ratios were found to be 0.25 and 0.5, respectively, suggesting asymmetric in-out boundary crossings with inward pointing normals inclined 75° and 63° with respect to the magnetic field vector. The transverse extent of these structures is estimated to be 3.5 km and 5.6 km, respectively, assuming a static model (see discussion below on the validity of the static assumption), which is of the order of the electron inertial length, $c/\omega_{pe} \approx 3$ km. The electron and ion data were too coarsely sampled to reliably determine whether their properties are consistent with the sense of these $E_{||}$ structures.

The 40-Hz electric field observations do not preclude the possibility that the $E_{||}$

signatures were caused by higher frequency oscillations. For example, the $E_{||}$ structures could represent the envelope of a more or less unipolar, higher frequency wave packet, as observed in the plasma sheet boundary [e.g., *Cattell et al.*, 1998b]. In addition, the rectification of waves with angular frequencies above the inverse plasma sheath-sphere RC time could induce DC offsets in the probe potential measurements [*Boehm et al.*, 1994], which could show up, in the transformed data, as a parallel electric field structure. This rectification effect is due to the nonlinear response of the detector to the higher frequency wave. To show that these two different effects are not causing the $E_{||}$ signatures, Figures 2(d)–2(f) display the components of the electric field constructed from data sampled at 1600 Hz through a 500 Hz low-pass filter. In addition to the broad, large-amplitude structures seen in the 40 Hz data, the burst data reveals the presence of short duration solitary-like structures of significant amplitude (200-300 mV/m), occurring in the interval from 0324:33.5UT to 0324:34.4 UT. The impulsive structures have significant power, both parallel and perpendicular to the magnetic field vector. Figure 2(g) shows a times series of the $E_{||}/E_{\perp}$ ratio that characterizes the entire interval. The interval over which the spiky structures occur only partially overlaps regions containing macroscopic $E_{||}$ structures, which suggests that the macroscopic $E_{||}$ structures are not the envelopes of unipolar, higher frequency wave packets, and are not caused by rectification effects. **Plate 3.**

To distinguish the nature of the broad $E_{||}$ events from the spiky structures, it is useful to perform a wavelet analysis. Plates 3(a)–3(c) display the time-frequency power spectra of the electric fields given in Figures 2(d)–2(f), respectively. The power spectra were based on a Morlet wavelet [e.g. *Torrence and Compo*, 1998], which is ideal for resolving localized structures. The dotted white lines at 120, 30, and 7.4 Hz in Plates 3(a)-(c) represent the H^+, He^+, and O^+ gyrofrequencies, respectively. The macroscopic structures are manifested in the frequency regime $\lesssim$ 10 Hz, whereas the spiky structures have peak power at frequencies near f_{H^+} and f_{He^+}. The transverse electric field has considerable broadband power in the north-south direction (see Plate 3(a)), with substantially less power in the east-west direction (see Plate 3(b)). A sharp separation of scales is apparent in the parallel component depicted in Plate 3(c). Namely, the power is substantially depressed at frequencies slightly above 10 Hz, which does not occur in the perpendicular components. **Figure 3.**

The spectral density of the electric field (in units of $(\mathrm{mV/m})^2/\mathrm{Hz}$) averaged over the interval from 0324:33.1 UT to 0324:34.6 UT are indicated by the solid curves in Figures 3(a)–3(c). The vertical lines Figures 3(a)–3(c) indicate the gyrofrequencies f_{H^+}, f_{He^+}, and f_{O^+}. The AC magnetic field search coil data are available for this event, however we saw no significant perturbations, with the search coil signal being indistinguishable from the background magnetic field noise observed in neighboring quiet regions. For completeness, the power spectra (dashed curves) of the search coil magnetic fields (in units of $(\mathrm{nT})^2/\mathrm{Hz}$) have been included in Figures 3(a)–3(c). The lack of any noticeable magnetic field perturbation associated with the electric field data suggests that the electric fields are electrostatic in character.

The electrostatic character and the near coincidence of the spectral peaks with the characteristic gyrofrequencies in Figures 3(a)–3(c) suggest that the spiky structures are H^+ and He^+ ion cyclotron waves, which have been commonly observed in the auroral acceleration region [e.g., *Mozer et al.*, 1977; *Kintner et al.*, 1979; *Cattell et al.*, 1991, 1998a]. The fact that the broad $E_{||}$ structures partially overlap the oxygen gyrofrequency regime suggests that the macroscopic $E_{||}$ structures may be the result of oxygen cyclotron fluctuations. However, we performed a time-of-flight analysis using potential measurements from opposing probes and found that the large scale structures are static structures convecting by the spacecraft at the spacecraft speed. The validity of an oxygen cyclotron description would require the wave vector to have a preferred alignment relative to the spacecraft trajectory, a scenario which is possible, but unlikely. Moreover, the large scale $E_{||}$ structures are not oscillatory in nature, but appear, in this example, nearly coincident with a pair of macroscopic, converging $E_\perp$ structures often called "electrostatic shocks".

Alfvén waves can have a significant parallel electric field component and can appear to be electrostatic, especially for structures that are sufficiently narrow in the direction transverse to the magnetic field [e.g., *Lysak and Lotko*, 1996; *Lysak*, 1998; *Stasiewicz et al.*, 2000, and references therein]. Thus it may be the case that the large amplitude macroscopic parallel electric fields are caused by kinetic Alfvén waves. This notion can be tested by establishing whether the ratio $\nu = V_A B_Y / E_X$ associated with the field signatures interest is consistent with the predictions of the kinetic Alfvén wave model. Over the frequency regime ($\lesssim$ 10 Hz) corresponding to the macroscopic parallel electric field signatures, the ratio $\nu_{\rm obs} = V_A B_Y / E_X$ was found to vary from 5×10^{-3} to $5{\times}10^{-2}$. The kinetic Alfvén wave expectation for the ratio ν_A is plotted as a function of V_e/V_A and $k_\perp c/\omega_{pe}$ in Figure 1 of the paper by *Lysak* [1998]. In this example the electron temperature varied from 0.5 to 1 keV and the density varied from roughly 0.5 to 10 cm^{-3} in the vicinity of the events. The perpendicular widths of the field structures were determined previously. Using these values we determined that $k_\perp c/\omega_{pe} \approx 2\pi c/(\omega_{pe} L_\perp)$ ranges from 3.0 to 10 and V_e/V_A ranges from 0.3 to 0.4. These values suggest an Alfvén wave expectation for the ratio $\nu_A \sim 0.4$ to 0.9, which is one to two orders of magnitude larger than $\nu_{\rm obs}$. Thus, we conclude that the kinetic Alfvén wave explanation for the occurrence of the macroscopic parallel electric field structures is not plausible in this case.

3.3. July 20, 1997 event

Plate 4.

Plate 4 illustrates another example of large amplitude parallel electric fields. The three hour averaged K_p was 2. Large $E_{||}$ events were observed at $\sim$ 1308:15 UT with peak amplitudes of 84 mV/m and 76 mV/m, respectively. The events are coincident with $E_\perp$ structures with respective amplitudes of 190 mV/m and 140 mV/m. The region was characterized by an upward field-aligned current with an amplitude of 0.14 μA/m^2 (slope of ΔB_Y illustrated in Plate 4e). The $E_{||}$ events occurred in moderately depressed density regions of ~1 cm^{-3} compared to the peak quiet region density of about ~50 cm^{-3} as is inferred from the $\Phi_{\rm SC}$ given in Plate 4d. The events are relatively narrow, characterized by spatial widths transverse to the magnetic field of 9 km (0.9 c/ω_{pe}) and 5 km (0.6 c/ω_{pe}), respectively. These events are particularly interesting because particle measurements were acquired during times concurrent with the large parallel field. Upward moving ions (see Plates 4g and 4h), and downgoing electrons (Plates 4i and 4j) are shown to be coincident with the $E_{||}$ structures. The parameter $\Phi_{\rm pl}$ given in Plate 4f suggests a ~ 1 keV potential drop below the S/C. **Plate 5.**

Cuts of the electron and ion distribution function aligned (red curve), opposed (blue curve), and perpendicular (magenta curve) to the magnetic field vector are exhibited in Plates 5a and 5b, respectively. The downward cut (blue curve) of the electron distribution function in Plate 5a is sharply peaked at 1 keV with a phase space density that is more than an order of magnitude larger than both the field-aligned (red curve) and perpendicular (magenta curve) cuts. Similarly, the upward cut (red curve) of the ion distribution is sharply peaked at 500-600 eV, with little or no phase space density in the downward and perpendicular cuts. The energy of the ion beam is consistent with the $\Phi_{\rm pl}$ expectation for the potential below the spacecraft. Estimates of the vertical extent of the parallel potential are roughly 10 km above and 5 km below the spacecraft, assuming a constant parallel electric field that is responsible for all of the electron and ion acceleration.

3.4. April 04, 1996 event

Plate 6.

As an illustration of one of the largest $E_{||}$ amplitudes encountered by Polar, Plate 6 depicts field and particle data for a southern crossing near local midnight on April 4, 1996, featured in an earlier study [*Mozer and Kletzing*, 1998]. The region is characterized by a K_p index of 2 and a uniform upward field-aligned current with an amplitude of 0.01 μA/m^2 (see Plate 6e). Polar enters a region of depleted density at ~2044:27 UT (see Plate 6d). The high to low density ratio is roughly 50. The perpendicular component of the electric field (see Plates 6a and 6b) is of small amplitude ($\sim$ 50 to 100 mV/m at the edges of the density cavity, and reaching much smaller values within the density cavity). The parallel electric field component is nearly zero, except at ~2044:46 UT, where the amplitude reaches 250 mV/m (Plate 6c). The $E_{||}/E_{\perp}$ ratio corresponding to the large parallel field signature is roughly 8. The plasma density associated with the large $E_{||}$ signature is about 0.07 cm^{-3}, which is an order of magnitude less than the 0.5 cm^{-3} peak density in the interval immediately following the $E_{||}$ signature. The perpendicular width of the parallel field is estimated at 0.9 km ($\sim$ $0.1c/\omega_{pe}$), which maps down to roughly 300 m at ionospheric altitudes.

Within the density cavity region (~2044:27-2044:45 UT), upgoing ion beams are observed (see Plates 6g and 6h). It is important to note that the upgoing ion beams are quite narrow in pitch angle and Hydra, with gaps in its angular sampling, captures the narrow beam occasionally through the interval, and only when one of the pairs of detectors is nearly aligned along the magnetic field line. This was the case for the samples taken at 2044:29, 2044:35, 2044:45, and 2044:47 UT. In all of the other ion sampling intervals, the angle between the nearest detector look direction and the magnetic field direction was too large ($\gtrsim 30°$), and thus ion beams (if present) were missed by HYDRA.

In contrast, the electron distribution is well resolved by the HYDRA detector. Plates 6i and 6j show that downgoing electrons are present inside the density cavity. The dropouts in the upgoing electron differential energy flux signify the existence of a parallel potential below the spacecraft, which prevents electrons of ionospheric origin from accessing this altitude. The electron and ion signatures coupled with the electric field observations inside the density cavity suggest that Polar is within an acceleration region characterized by a parallel potential that is distributed over a large spatial extent (thousands of kilometers).

HYDRA's sampling time resolution is too coarse to establish the particle properties within the large amplitude parallel electric field structure, though there are upgoing ions and downgoing electrons in the vicinity of the $E_{||}$ event with peak beam energies of about 0.5 kV. This suggests a parallel potential that is distributed over a few kilometers.

Figure 1d displays one possible model of the potential distribution that can explain these observations. Within the density cavity, the equipotential contours are envisioned to be distributed over a large spatial extent, whereas at the outgoing edge of the density cavity the potential contours are kinked or S-shaped. This event illustrates the complex nature of the auroral acceleration proper, namely, the potential can be distributed over a large spatial extent and also be sheath-like in structure within a given current region. As to what determines whether the potential is highly localized in space or not is still not well understood. A detailed analysis suggests that ambipolar effects may be important (see discussion below in section 5).

3.5. October 13, 1996 event

Plate 7.

In contrast with the nonoscillatory, macroscopic $E_{||}$ structures discussed in Sections 3.1–3.4, we provide, in this section, an example with large parallel and perpendicular oscillations which appear to be those of oxygen cyclotron waves. The event occurred near local midnight on October 13, 1996 at an altitude of ~6000 km. The K_p index was 2-, suggesting relatively quiet global auroral activity. Plate 7 summarizes the particle and field data for this event. This example contains $E_{||}$ fluctuations (Plate 7c) with peak amplitudes ranging from 50-200 mV/m. In this event the density makes a transition from ~20 cm^{-3} to roughly 10^{-3} cm^{-3} as inferred from Φ_{SC} given in Plate 7d. The slope of ΔB_Y (Plate 7 e) suggests that the $E_{||}$ fluctuations occur in a region of upward field aligned current. The $E_{||}$ amplitude is oscillatory in nature, and becomes most pronounced from 1318:31 to 1318:33 UT, which corresponds to a region of very low density (or large negative $\Phi_{\rm pl}$ illustrated in Plate 7d). Intense field-aligned ion beams with mean energy of $\sim$ 1 keV are shown to be concurrent with the low density region. The amplitude and energy of the ion beams is consistent with $\Phi_{\rm pl}$. At this time resolution, the electrons were not well sampled along **B** in the density cavity, although the distribution function in $v_{||} - v_{\perp}$ space (not shown) is consistent with precipitating electrons. **Figure 4.**

To better establish the properties of the fluctuations, we separated the higher frequency components from the macroscopic structure by boxcar averaging the electric field components depicted in Plates 7a–7c using a sliding boxcar window of 6 points (0.4 sec resolution) and then subtracting this result from the unaveraged field components. The resulting detrended AC components of the electric field are given in Figures 4a–4c. The corresponding macroscopic fields are depicted in Figures 4d–4f. The spacecraft potential profile is provided in Figure 4g, as a reference. The parallel fluctuations are coincident with perpendicular fluctuations of similar amplitude. Throughout most of the interval, parallel spikes depicted in Figure 4c are accompanied by spikes in either one or both of the perpendicular fields depicted in Figures 4a and 4b. The correlation coefficient between the magnitudes of the parallel and perpendicular AC electric fields was 0.5. This strong correspondence suggests that the perpendicular and parallel fluctuations are from the same mode. In addition to the large $E_{||}$ fluctuations, there exists large amplitude macroscopic parallel electric fields which range in amplitude from 40 mV/m to 70 mV/m occurring at $\sim$ 1318:30 UT and $\sim$ 1318:32, respectively (see Figure 4f). The respective $E_{||}/E_{\perp}$ ratios are found to be 0.6 and 1.0. The macroscopic events are characterized by a transverse width of roughly 2 km. In stark contrast with the parallel field oscillations, the macroscopic fields are not oscillatory in nature, appearing as a unipolar signature of a sense to accelerate ions upwards and electrons downward. This unipolar feature is a recurring property of the $E_{||}$ events that make up this database. **Figure 5.**

To provide insight into the identity of these fluctuations, Figures 5a–5c display the power spectra of the electric field components depicted in Plates 7a–7c, within the cavity. The solid curve in each of the figures represents the power spectra of the unaveraged electric field and the dotted curve represents the power spectra of the detrended AC electric field components. The peaks in all 3 components of the field near 3 Hz reflects the macroscopic structure. In addition, all three components show a significant peak at about 7-8 Hz, which is roughly at the oxygen gyrofrequency f_{O^+} indicated by the solid vertical line. The near coincidence suggests that these oscillations are consistent with oxygen cyclotron waves. The occurrence of oxygen cyclotron waves suggests the presence of O^+ with significant density. Moreover, the power spectra indicates that the parallel electric field component has significant power. Oxygen cyclotron waves with large parallel fields are expected to cause significant electron flux modulations, which ultimately produce flickering aurora. It is important to note that the peaks at the oxygen cyclotron frequency should be viewed with caution. Depending on the filter roll-off, significant power at up to twice the Nyquist frequency could contaminate the lower frequency components. Thus, it may be the case that the power at 7-8 Hz could be due to a combination of O^+ and He^+ cyclotron modes (which if present should occur at $\sim$ 30 Hz). Additional peaks in the power spectra occur near the Nyquist frequency for both the FAC Ex and Ez components of the electric field. We do not have a reliable explanation for these peaks at this time.

4. Statistical Properties

Polar provides nearly uniform invariant latitude (Λ) and magnetic local time (MLT) coverage of the southern auroral zone over the three year sampling period. In three years of EFI data, with a total of about 3000 inbound and outbound crossings of the auroral zone, roughly 60 events or 2% of the crossings contain large amplitude parallel electric fields. This low observation rate is consistent with their typical vertical extents which are inferred to be, at most, a few tens of kilometers. In the following subsections, we compare the properties of the $E_{||}$ events with other parameters that characterize the auroral acceleration region.

4.1. Geographic Location of $E_{||}$ Samples

Figure 6.

Figure 6a shows the geographic location of the events that make up this database. The events trace out a pattern characteristic of the auroral zone location in Λ and MLT in Figure 6a. However, the events are clustered in the premidnight quadrant, with substantially fewer events near local noon. This tendency is qualitatively similar to the distribution of inverted-V electron events [*Lin and Hoffman*, 1979], ion beams [*Gorney et al.*, 1981], and electrostatic shocks associated with ion beams [*Bennett et al.*, 1983; *Redsun et al.*, 1985] observed in the auroral zone.

Figure 6b shows a histogram of the altitudes at which the $E_{||}$ events were observed by Polar. The altitudes ranged from 0.8-1.5 R_{E}, which corresponds to 5000 to 9600 km. The limited altitude range over which the parallel electric fields occurred is artificial and reflects the altitudes sampled by Polar in the southern auroral zone over the first three years of its mission. Thus, large amplitude parallel electric fields may exist at altitudes above and below those sampled in this study. Figure 6b suggests that the frequency of occurrence of macroscopic parallel electric fields with amplitudes greater than our acceptance criteria of 25 mV/m decreases with increasing altitude. These results are consistent with the results of a recent survey [*Mozer and Hull*, 2001] of Polar data which found no evidence for large amplitude parallel electric fields at much higher altitudes (2-6 R_{E}). Our results together with those of *Mozer and Hull* [2001] suggest that the large amplitude macroscopic parallel electric fields are a property of the low-altitude portion of the auroral acceleration region.

4.2. Characteristic Amplitudes

Figure 7.

A summary of the characteristic electric field amplitudes of the events that make up this database is given in Figure 7a–7d. Figure 7a gives the distribution of the peak amplitude of the parallel electric events. The most probable peak value of the parallel electric field, $E_{||_m}$, is found to be 70 mV/m, though much higher values are possible. The cutoff at low amplitudes is artificial and reflects the minimum amplitude of $E_{||}$ selected for this study. Figure 7b is a histogram of the amplitude of the perpendicular electric field field coincident with the peak parallel electric field of each event that makes up this study. Figure 7c is a histogram of the ratio $\epsilon = E_{||}/E_{\perp}$ and Figure 7d is a scatter plot of $E_{||}$ and $E_{\perp}$. The solid lines in Figure 7d represent different values of ϵ. The typical ϵ is 0.4 which indicates that large $E_{||}$ events are concurrent with much larger $E_{\perp}$, although there are several events with much larger ratios. The ratio ϵ provides information on the geometries of the potential well encountered by Polar. Many of the events occur in the transition between high and low density plasma, with some events occurring within the acceleration proper. The typical orientation of the boundary normal characterizing the transition region is inclined at an angle $\alpha = \tan^{-1}(1/\epsilon) = 70°$. Values for $\epsilon \gtrsim 0.4$ are unlikely to be explained by uncertainties in the projection of a large, purely perpendicular field. Such a scenario would require errors of $\gtrsim 20°$ in the magnetic field direction.

Figure 8.

Figure 8a-c shows the altitude dependence of the magnitudes of $E_{||}$, $E_{\perp}$, and ϵ, respectively. There is no clear dependence between the magnitude of $E_{||}$ and altitude, though there is a hint that the biggest $E_{||}$ events are confined to lower altitudes. Figure 8c suggests that the largest $E_{||}/E_{\perp}$ ratios occur at the lower altitudes. This tendency is an indication of the geometrical sampling of the potential wells that make up this database and is consistent with the canonical electrostatic U-shaped model of the electron acceleration region, where the electric field is primarily perpendicular to the magnetic field at high altitudes and primarily field-aligned at low altitudes.

4.3. Comparisons with Parallel Current Density

Figure 9.

We explored whether or not the size of the parallel electric field is controlled by parallel current density. An appropriate measure of the current is the ratio $J_{||}/B$ which for a given event should be a constant along a magnetic field line, provided the system is time stationary and the perpendicular current density is zero. The $J_{||}$ was empirically inferred from $\nabla \times \Delta\mathbf{B}_{\rm av} = \mu_0 \mathbf{J}$, where $\Delta\mathbf{B}_{\rm av}$ is the spin period averaged perturbation vector magnetic field and $\mathbf{J}$ is the current density. Linear interpolation was used to determine $J_{||}$ at the time $E_{||}$ occurred. Figure 9a–9c compare $J_{||}/B$ with altitude, $E_{||}$, and $E_{\perp}$. Figure 9a indicates that there is no apparent altitude dependence on the current. The most probable value for $J_{||}/B$ was found to be 2.0×10^{-11} A/(m^2 nT). There are events that have negative values, although a closer inspection of these events suggests that they may be explained by coarse sampling of $\Delta\mathbf{B}_{\rm av}$ in a rapidly changing current region. Nevertheless, $\Delta\mathbf{B}_{\rm av}$ provides a reliable estimate for $J_{||}$ in an average sense. Figures 9b and 9c show no apparent $E_{||}$ and $E_{\perp}$ dependence with current. However, there is a correlation between the direction of current and the direction of the parallel electric field, namely upward parallel electric fields are associated with upward pointing field-aligned current. The statistical correlation of the current sense with sense of the parallel electric field argues against an explanation of our results from random or spurious electric fields; with such an explanation there should be no preference for the direction of current.

4.4. $E_{||}$ Anticorrelation with Density

Theoretical models of the auroral acceleration region [e.g., *Knight*, 1973; *Rönmark*, 1999] predict, among other things, a relationship between the the parallel electric field and the plasma density. Recent particle and field observations at higher altitudes [*Mozer and Hull*, 2001] also suggest the importance of the plasma density in determining the presence of parallel potential drops in the auroral zone . In particular, *Mozer and Hull*

[2001] demonstrated that upgoing ions, which indicate significant parallel potential drops below the spacecraft, are not associated with variations in the current, but coincided with regions of depressed plasma density. Thus one might suspect that the large amplitude parallel electric fields discussed in this paper should depend on the plasma density.

Figure 10.

Figure 10 compares $E_{||}$ with Φ_{SC} or equivalently with the plasma density N. The density dependence depicted in Figure 10 was determined from the relation given by *Scudder et al.* [2000]. The comparisons in Figure 10 indicate that the amplitude of $E_{||}$ increases with increasingly larger negative values of Φ_{SC} or equivalently with smaller values of the plasma density. The best fit slope and intercept is found to be -0.05 km and -2.9 V, respectively, and the linear correlation coefficient is -0.69. The strong $E_{||}$-Φ_{SC} anticorrelation illustrated in Figure 10 suggests a strong anticorrelation between $E_{||}$ and the $\log(N)$. It is not guaranteed that our statistical result is reflective of the local dependence between the plasma density and the electric field along a magnetic flux tube of force. Nevertheless, it is suggestive of the average variation of the parallel electric field in relation to variations in the plasma density, given that the events sampled covers a broad altitude range. Such a dependence places a rather strict constraint on the mechanism or mechanisms responsible for supporting such large parallel electric fields. We interpret the anticorrelation to be a manifestation of an ambipolar response of the plasma at the interface between the low density magnetospheric plasma and the high density ionospheric plasma. The net result is a parallel electric field with a sense to accelerate electrons downward and ions upward to maintain current balance and quasineutrality (see discussion below in section 5 for more details).

4.5. Electric Field Transverse Widths

Figure 11.

Earlier studies [e.g., *Mozer et al.*, 1980; *Mozer*, 1981] have investigated the spatial scales of auroral zone electric fields. In particular, the study by *Mozer et al.* [1980]

suggested the presence of two spatial scale sizes for the perpendicular electric fields: (1) a broad scale of about a few degrees in invariant latitude (e.g., a few hundred kilometers at ionospheric altitudes) associated with the entire turbulent auroral zone electric field region, which may encompass several converging pairs of perpendicular fields, and (2) a much thinner scale $W'_{E\perp}$ ranging from 0.01° to 0.1° in invariant latitude (e.g., from 1 to 10 km at ionospheric altitudes) associated with a given pair of converging perpendicular electric fields. Our study focuses on the thinner spatial scale structures, with the perpendicular electric field transverse widths being roughly $W_{E\perp} \approx W'_{E\perp}/2$.

In this section we summarize the properties of the transverse widths $W_{E||}$ and $W_{E\perp}$ of the macroscopic parallel and perpendicular electric fields, respectively, that comprise this database. The $W_{E||}$ is defined as the full width at half maximum of the $E_{||}$ signature. Many of the $E_{||}$ structures occurred nearly simultaneously with an $E_{\perp}$ structure which may be broader or narrower. However, a few cases (few percent) occurred in the center of converging pairs of $E_{\perp}$. Thus, we defined $W_{E\perp}$ as the full width at half maximum of the $E_{\perp}$ structure nearly coincident with a given $E_{||}$ structure, or as the full width at half maximum of the nearest $E_{\perp}$ structure in those cases with $E_{||}$ at the center of converging pairs of $E_{\perp}$. The macroscopic electric field structures were assumed to be convecting by the spacecraft at the orbital velocity in converting from time to spatial coordinates. Such an approximation was found to be valid for one of the examples discussed above via time-of-flight analyses of burst mode potential measurements from opposing sphere pairs (e.g., see the discussion in Section 3.2).

Histograms of $W_{E||}$ and $W_{E\perp}$ are given in Figures 11a and 11b, respectively. The $W_{E||}$ range in value from 0.5 to 26 km with a peak value at 1 km and median value of 4 km. The distribution of $W_{E\perp}$ is somewhat broader than the $W_{E||}$ distribution, characterized by $W_{E\perp}$ ranging from 0.5 to 30 km, and peak and median $W_{E\perp}$ values of at 1 km and 6 km, respectively. We imposed a lower spatial bound 0.5 km in selecting the $E_{||}$ events for this data set. The electric field estimates for events with spatial sizes much smaller than 0.5 km can be significantly impacted by finite wavelength effects in addition to possible density and temperature gradient effects. Thus, the lower cutoff value is artificial and smaller widths are possible, though we feel that they cannot be measured reliably by EFI.

The $W_{E\perp}$ in our study mapped to ionospheric altitudes corresponds to 0.17 km to 10 km, which is roughly consistent with the 0.5 to 5 km range of widths inferred from the study by *Mozer et al.* [1980], although our estimates map to somewhat thinner structures at the ionosphere. The range of $W_{E||}$ corresponds to roughly 0.17 km to 8 km at ionospheric altitudes, with a distribution that is in rough correspondence with the distribution that characterizes the smallest scale sizes of discrete auroral arcs [e.g., *Maggs and Davis*, 1968]. Ultimately, the fine structure of auroral forms are connected with the detailed properties of the electron precipitation. Localized pockets of intense $E_{||}$, such as those presented in this paper, could lead to fine scale enhancements of the energy flux of inverted-V precipitating electrons and hence to fine scale variations in discrete auroral arcs.

Figures 11c and 11d depict distributions of $W_{E||}$ and $W_{E\perp}$, respectively, normalized by the electron inertial length ($L_e = c/\omega_{pe}$). Estimation of ω_{pe} requires knowledge of the local plasma density, which was estimated from direct measurements of the spacecraft potential using the density-spacecraft voltage relation developed by *Scudder et al.* [2000]. Although somewhat broad, the normalized distributions given in Figures 11c and 11d show that the $W_{E||}$ and $W_{E\perp}$ are typically the order of the electron inertial length. Other characteristic spatial lengths of interest are the electron Debeye length λ_e and proton gyroradius r_p. At these altitudes, $c/\omega_{pe} \sim 20\lambda_e \sim 20r_p$ (assuming 1 keV protons and an electron temperature ~1 keV). Thus the typical widths of the fields are of the order of $20\lambda_e$ or $20r_p$.

4.6. Association with Global Auroral Activity

Figure 12.

Earlier observational studies [*Bennett et al.*, 1983; *Reiff et al.*, 1993] found that more intense perpendicular electric fields at low-altitudes tended to be associated with higher values of K_p. We explored the relationship between K_p and the amplitudes of $E_{||}$. Figure 12a shows the distribution of three hour averaged K_p values that characterize this data set. The K_p values range from 0 to 6 with a typical value of 2, which is characteristic of auroras during quiet times. The scatter plot displayed in Figure 12b shows no apparent dependence between K_p and $E_{||}$ amplitudes, except that the $E_{||}$ events that make up this data set tend to be more commonly associated with less active aurora. The lack of events at higher values of K_p could be a reflection of the typical global auroral activity associated with the three year period over which this data set was sampled, which started just after solar minimum. Whether there is any dependence with K_p can not be reliably determined with our current data set. Nevertheless, the large amplitude $E_{||}$ events in our database are not a byproduct of active aurora. Our database suggests that large amplitude parallel fields are a common feature of the typical state of the auroral acceleration region.

5. Discussion

The results of the individual case studies together with the statistical results provide important clues to understanding the mechanism or mechanisms that support these large amplitude macroscopic parallel electric fields. The statistical results of this paper suggest that the macroscopic parallel electric fields are directed upward and are intimately connected with the maintenance of an upward directed parallel current. The parallel electric fields were shown to be rather localized in space, with typical widths which are of the order of the electron inertial length. The resulting parallel potential has been inferred to extend over roughly tens of kilometers. The tendency for the parallel electric fields to occur at the boundary separating high and low density plasma may be an indication that they occur in response to the plasma's inability to carry the current in the transition between magnetospheric and ionospheric plasmas. The properties of the parallel electric field are intimately related to the way momentum is imparted to the current carriers, the process of which may depend on effects such as pressure gradients, inertia, and anomalous resistivity as embodied in the generalized Ohm's law. A convenient expression for the steady state electric field that is equivalent to the generalized Ohm's law is the steady state electron momentum equation given by the following expression:

$$\mathbf{E} = -\frac{\mathbf{U_e} \times \mathbf{B}}{c} - \frac{1}{eN_e}\nabla \cdot \mathbf{P_e} - \frac{m_e}{e}\mathbf{U_e} \cdot \nabla \mathbf{U_e} + \eta \mathbf{J}, \tag{1}$$

where m_e is the electron mass, c is the speed of light, e is the electron charge, N_e is the electron density, $\mathbf{U_e}$ is the electron bulk velocity, $\mathbf{P_e}$ is the electron pressure tensor, η is the anomalous resistivity, and $\mathbf{J}$ is the current density. The first term in (1) often denoted the unipolar electric field term has no contributions to the parallel electric field, the second term is the ambipolar electric field term, the third represents electron inertia effects, and the fourth term reflects anomalous resistivity effects. The statistical anticorrelation between the amplitude of the parallel electric field and the logarithm of the density signifies the importance of gradients in the plasma density in determining the parallel electric field. The two terms in (1) that involve gradients in density that can support parallel electric fields are electron inertia and the ambipolar terms. In the following we will discuss the implications of electron inertia and ambipolar effects on localized macroscopic parallel electric fields.

5.1. Electron Inertia

The more or less confinement of $E_{||}$ and $E_{\perp}$ to widths which are of the order of the electron inertial length suggests the possibility that inertial effects may be important in supporting the parallel field and establishing its spatial scale. Recent theoretical studies have suggested that electron inertia alone can support the parallel electric fields responsible for accelerating electrons to keV energies [*Rönmark*, 1999]. According to *Rönmark* [1999], the parallel electric field determined by electron inertia can be expressed by the following:

$$E_{||} \sim -\frac{m_e}{e} U_{e||} \frac{\partial U_{e||}}{\partial S_{||}}, \tag{2}$$

where m_e is the electron mass, $U_{e||}$ is the electron bulk speed parallel to the magnetic field vector (which is different from the electron beam speed used to infer the potential from the electron distribution function), and $S_{||}$ is the arc length along the magnetic field. Using the field line conservation constraint $\Gamma = N_e U_{e||}/B = const$, we can express (2) in terms of gradients in the density and the magnetic field as follows:

$$E_{||} \sim \frac{m_e}{e} \Gamma^2 \Big[\frac{B^2}{N_e^3} \frac{\partial N_e}{\partial S_{||}} - \frac{B}{N_e^2} \frac{\partial B}{\partial S_{||}} \Big]. \tag{3}$$

The gradients in the plasma density associated with the parallel electric fields are much larger than the magnetic field gradient over the tens of kilometer distances these parallel field occur. This suggests that the first term should dominate yielding an electric field which is in the same direction as the density gradient. The density increases with decreasing altitude. Consequently, the electric field is predicted to point downward, which is contrary to the observations. Thus it appears that the electron inertial effects can not explain these localized large amplitude parallel electric fields. However, it is important to mention that such arguments can not rule out electron inertial effects as a possible explanation for the weak parallel electric fields responsible for kV potential drops distributed over thousands of kilometers at higher altitudes, provided that it can be demonstrated that $|B/\nabla B| > |N_e/\nabla N_e|$.

5.2. Ambipolar Effects

The ambipolar term of the electron momentum equation can support parallel electric fields in regions of sharp density and temperature gradients. The current observations are unable to unambiguously determine whether the density gradient along the field line is larger than, smaller than, or of the same order as the temperature gradient. However, the transverse observations inside and outside the density cavities reveal much sharper transitions in the density than in the temperature on the short scales over which the electric fields occur. The electron density outside the cavity, which is dominated by a mixture of ionospheric and magnetospheric components, is much larger than the plasma inside the cavity which is primarily composed of magnetospheric electrons. Typically, the ratios between the density outside and the density inside the cavity were found to be N_{eI}/N_{eMS} ~10 to 100 and can be as large as 1000 (in our study). An examination of the electron temperature changes across these cavities reveals a much weaker transition, namely, the ratio between electron temperature outside to the electron temperature inside was observed (when available) to be roughly $T_{eI}/T_{eMS} \sim 0.3$ to 0.5. Although such a dependence is not necessarily guaranteed along the magnetic field, it is reasonable to assume that the local density gradient along the field line is much larger than that of temperature. In this approximation the parallel electric field can be expressed as

$$E_{||} \approx -\frac{k_b T_e}{e} \frac{\partial \ln(N_e)}{\partial S_{||}}, \tag{4}$$

where k_b is the Boltzmann constant, T_e is the electron temperature, N_e is the electron density, and $S_{||}$ is the arc length along the magnetic field vector. This expression predicts that the parallel electric field is in the opposite direction of the density gradient. Thus, a downward directed density gradient implies an upward directed parallel electric field which is consistent with our results.

Expression (4) can be rewritten to yield an order of magnitude estimate of the altitudinal extent of the parallel potential as follows:

$$\delta S_{||} \sim \frac{k_b T_e}{e E_{||}} \ln\left(\frac{N_{eI}}{N_{eMS}}\right) \tag{5}$$

Using typical values for electron temperature and the density ratio, (5) yields $\delta S_{||} \sim 20$ to 50 km for a 100 mV/m parallel electric field. This result is in reasonable agreement with altitudinal extents previously estimated from the measured parallel electric field and parallel potential drop inferred from the electron and ion beam energies.

The typical transverse width of the perpendicular field can be also be estimated. For a monotonic potential ramp characteristic of the transverse high and low density transition, the full widths at half maximum of $E_\perp$ is in a sense a measure of the perpendicular scale over which the potential drop is distributed. Assuming that the geometry is locally planar and that the ambipolar effects determine the electric field, the parallel length is related to the perpendicular width $W_{E_\perp}$ by $\delta S_{||}/W_{E_\perp} = 1/\epsilon$. Thus, we obtain an expression for the perpendicular width of the following form:

$$W_{E_\perp} \sim \epsilon \frac{k_b T_e}{e E_{||}} \ln\left(\frac{N_{eI}}{N_{eMS}}\right) \tag{6}$$

Using the peak value for $\epsilon \sim 0.4$ yields $W_{E_\perp}$ ~8 for a density ratio of 10 and a 1keV electron temperature. This compares favorably with the median value of $W_{E_\perp}$ which was found to be 6 km.

Finally, the statistical anticorrelation between the parallel electric field and the plasma density can be explained by the following heuristic arguments. If on average the parallel electric field measurements were taken near the center of the parallel potential ramp, the density can be approximated as $\ln N^* \approx (\ln N_I + \ln N_{MS})/2)$. Substituting this into (5), we get a relation between the parallel electric field and the locally measured density as follows: $E_{||}{}^* \approx -2(k_b T_e/e)[\ln N^* - \ln N_I]/\delta S_{||}$. Thus, with all other things being equal for different events, a smaller value of N^* will give rise to a larger $E_{||}{}^*$. This expression is just approximate, and breaks down when Polar is traversing the parallel electric field region near the top or bottom of the region. Physically, the statistical anticorrelation is viewed as a manifestation of an ambipolar parallel electric field, the strength of which depends on the sharpness of the density transition along the field-line.

These results suggest that the ambipolar term of the generalize Ohm's law provides a feasible explanation for both the parallel and perpendicular electric field structures associated with the sharp density transitions. However, unambiguous determination requires measurements along the magnetic field. Not precluded from this analysis is the possibility that the parallel potential associated with these large amplitude fields are the results of significant violations of quasineutrality (e.g., a sheath effect) often observed in experimental devices and considered in several theoretical studies. The parallel electric field amplitude is likely to be a lower bound on the maximum field that can occur along the field line. Much larger fields can occur along the field line characteristic of a sheath potential as suggested in more recent observational [*Mozer and Hull*, 2001] and theoretical models [*Ergun et al.*, 2000]. It may be the case that the parallel electric fields discussed in this study are characteristic of a presheath (a region where the quasineutral approximation is valid).

6. Conclusions

This paper presents the first statistical study of large amplitude, macroscopic parallel electric fields in the upward current portion of the southern auroral zone at altitudes ranging from $0.8R_{\mathrm{E}}$ to $1.5R_{\mathrm{E}}$. We found 64 events characterized by $E_{||}$ ranging in amplitude from about 25 mV/m to 300 mV/m. Moreover, $E_{||}$ represents a significant fraction of the total electric field strength (the $E_{||}/E_{\perp}$ ratios range from ~ 0.25 to O(1)). Many of the parallel electric field structures occur at the edges of converging pairs of perpendicular electric field structures (electrostatic shocks). The $E_{||}$ structures are associated with the upward current, tending to occur within or near regions containing upgoing ions and downgoing electrons. The frequency of occurrence of these large amplitude parallel electric field falls off significantly with altitude, suggesting that these parallel electric fields are a property of the low-altitude portion of the auroral acceleration region. We find no apparent correlation between the magnitude of $E_{||}$ and altitude, current, and K_p, although there is a suggestion that the largest $E_{||}/E_{\perp}$ ratios are confined to lower altitudes. The large parallel electric fields imply significant parallel potential drops that are rather localized in altitude (e.g., tens of kilometers as opposed to $\sim 10^3$ km). The $E_{||}$ structures have spatial widths that range from ~ 1.0 to 20 km which map to 100 m to 2 km at ionospheric altitudes, with a distribution that is in rough correspondence with the distribution that characterizes the smallest scale sizes of discrete auroral arcs [e.g., *Maggs and Davis*, 1968]. Thus, the observed $E_{||}$ could be a source of small-scale auroral structures embedded in broad arcs. The spatial widths that characterize the $E_{||}$ signatures are typically of the order of the electron inertial length. We tested the kinetic Alfvén wave expectation of the parallel and perpendicular fields and demonstrated that at least for the example tested the Alfvén explanation does not appear to be feasible. A detailed analysis suggests that these large amplitude parallel electric fields are probably the result of an ambipolar response of the plasma to sharp gradients density at the interface separating the cold, dense ionospheric plasma from the hot, tenuous magnetospheric plasma.

Acknowledgments. We thank C. T. Russell for the generous free use of the Polar magnetometer data. The work at UC Berkeley was supported by NASA grant 5-3182. Partial support for this work for J.D.S. from NASA grant 5-7883 is also acknowledged.

References

Bennett, E. L., M. Temerin, and F. S. Mozer, The distribution of auroral electrostatic shocks below 8000-km altitude, *J. Geophys. Res.*, *88*, 7107–7120, 1983.

Boehm, M. H., C. W. Carlson, J. P. McFadden, J. H. Clemmons, R. E. Ergun, and F. S. Mozer, Wave rectification in plasma sheaths surrounding electric field antennas, *J. Geophys. Res.*, *99*, 21,361–31,374, 1994.

Cattell, C., et al., The association of electrostatic ion cyclotron waves, ion and electron beams and field-aligned currents: FAST observations of an auroral zone crossing near midnight, *Geophys. Res. Lett.*, *25*, 2053–2056, 1998a.

Cattell, C. A., F. S. Mozer, I. Roth, R. R. Anderson, R. C. Elphic, W. Lennartsson, and E. Ungstrup, ISEE 1 observations of electrostatic ion cyclotron waves in association with ion beams on auroral field lines from $\sim$2.5 to 4.5 R_{E}, *J. Geophys. Res.*, *96*, 11,421–11,439, 1991.

Cattell, C. A., J. R. Wygant, J. Dombeck, F. S. Mozer, M. A. Temerin, and C. T. Russell, Observations of large amplitude parallel electric field wave packets at the plasma sheet boundary, *Geophys. Res. Lett.*, *25*, 857–860, 1998b.

Cattell, C. A., et al., Comparisons of Polar satellite observations of solitary wave velocities in the plasma sheet boundary and the high altitude cusp to those in the auroral zone, *Geophys. Res. Lett.*, *26*, 425–428, 1999.

Ergun, R. E., C. W. Carlson, J. P. McFadden, F. S. Mozer, and R. J. Strangeway, Parallel electric fields in discrete arcs, *Geophys. Res. Lett.*, *27*, 4053–4056, 2000.

Gorney, D. J., A. Clarke, D. Croley, J. Fennell, J. Luhman, and P. Mizera, The distribution of ion beams and conics below 8000 km, *J. Geophys. Res.*, *86*, 83–89, 1981.

Gurnett, D. A., et al., The Polar plasma wave instrument, *Space Sci. Rev.*, *71*, 597–622, 1995.

Harvey, P., et al., The electric field instrument on the Polar satellite, *Space Sci. Rev.*, *71*, 583–596, 1995.

Kintner, P. M., M. C. Kelley, R. D. Sharp, A. G. Ghielmetti, M. Temerin, C. Cattell, P. F. Mizera, and J. F. Fennell, Simultaneous observations of energetic (keV) upstreaming ions and electrostatic hydrogen cyclotron waves, *J. Geophys. Res.*, *84*, 7201–7212, 1979.

Knight, S., Parallel electric fields, *Planet. Space Sci.*, *21*, 741–750, 1973.

Lin, C. S., and R. A. Hoffman, Characteristics of the inverted-V event, *J. Geophys. Res.*, *84*, 1514–1524, 1979.

Lysak, R. L., The relationship between electrostatic shocks and kinetic Alfvén waves, *Geophys. Res. Lett.*, *25*, 2089–2092, 1998.

Lysak, R. L., and W. Lotko, On the dispersion relation for shear Alfvén waves, *J. Geophys. Res.*, *101*, 5085–5094, 1996.

Maggs, J. E., and T. N. Davis, Measurements of the thickness of auroral structures, *Planet. Space Sci.*, *16*, 205–209, 1968.

Mozer, F. S., ISEE 1 observations of electrostatic shocks on auroral zone field lines between 2.5 and 7 Earth radii, *Geophys. Res. Lett.*, *7*, 823–826, 1981.

Mozer, F. S., and A. Hull, The origin and geometry of upward parallel electric fields in the auroral acceleration region, *J. Geophys. Res.*, *106*, 5763, 2001.

Mozer, F. S., and C. A. Kletzing, Direct observation of large, quasi-static, parallel electric fields in the auroral acceleration region, *Geophys. Res. Lett.*, *25*, 1629–1632, 1998.

Mozer, F. S., C. W. Carlson, M. K. Hudson, R. B. Torbert, B. Parady, J. Yatteau, and M. C. Kelley, Observations of paired electrostatic shocks in the polar magnetosphere, *Phys. Rev. Lett.*, *38*, 292–295, 1977.

Mozer, F. S., C. A. Cattell, M. K. Hudson, R. L. Lysak, M. Temerin, and R. B. Torbert, Satellite measurments and theories of low altitude auroral particle acceleration, *Space Sci. Rev.*, *27*, 155–213, 1980.

Redsun, M. S., M. Temerin, and F. S. Mozer, Classification of auroral electrostatic shocks by their ion and electron associations, *J. Geophys. Res.*, *90*, 9615–9633, 1985.

Reiff, P. H., G. Lu, J. L. Burch, J. D. Winningham, L. A. Frank, J. D. Craven, W. K. Peterson, and R. A. Heelis, On the high- and low-altitude limits of the auroral electric field region, in *Auroral Plasma Dynamics*, *Geophys. Monogr. Ser.*, vol. 80, edited by R. L. Lysak, pp. 143–154, AGU, Washington, D. C., 1993.

Rönmark, K., Electron acceleration in the auroral current circuit, *Geophys. Res. Lett.*, *26*, 983–986, 1999.

Russell, C. T., R. C. Snare, J. D. Means, D. Pierce, D. Dearborn, M. Larson, G. Barr, and G. Le, The GGS/Polar magnetic fields investigation, *Space Sci. Rev.*, *71*, 563–582, 1995.

Scudder, J., et al., Hydra- a three-dimensional electron and ion hot plasma instrument for the Polar spacecraft of the GGS mission, *Space Sci. Rev.*, *71*, 459–495, 1995.

Scudder, J. D., X. Cao, and F. S. Mozer, Photoemission current-spacecraft voltge relation: Key to routine, quantitative low-energy plasma measurements, *J. Geophys. Res.*, *105*, 21,281–21,294, 2000.

Stasiewicz, K., et al., Small scale Alfvénic structure in the aurora, *Space Sci. Rev.*, *92*, 423–533, 2000.

Temerin, M., K. Cerny, W. Lotko, and F. S. Mozer, Observations of double layers and solitary waves in the auroral plasma, *Phys. Rev. Lett.*, *48*, 1175–1179, 1982.

Torrence, C., and G. P. Compo, A practical guide to wavelet analysis, *Bull. Amer. Meteor. Soc.*, *79*, 61–78, 1998.

J. W. Bonnell, A. J. Hull and F. S. Mozer, Space Science Laboratory, University of California, Berkeley, CA 94720

J. D. Scudder, Department of Physics and Astronomy, University of Iowa, Iowa City, IA 52242

Received ____________________; revised June 25, 2001

This manuscript was prepared with AGU's LaTeX macros v4, with the extension package 'AGU^{++}' by P. W. Daly, version 1.5f from 1998/07/16.

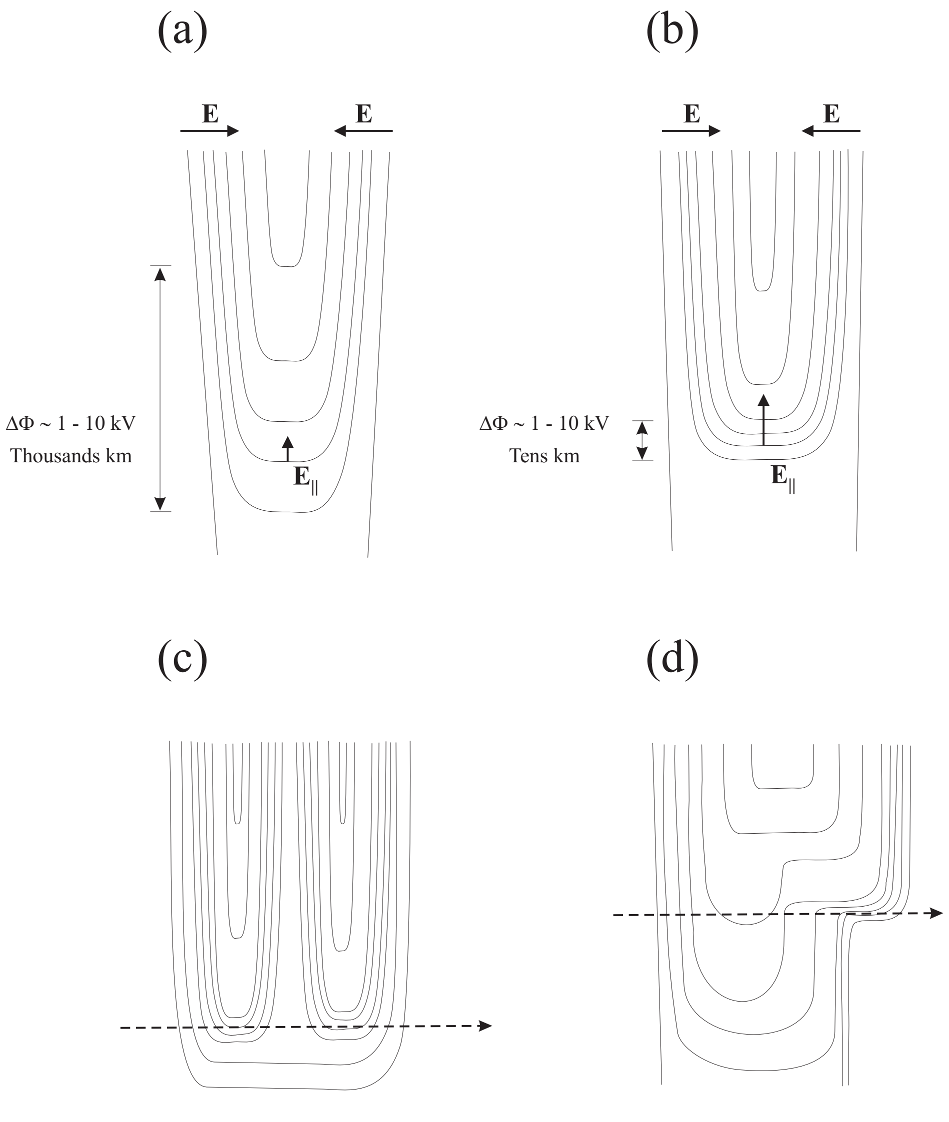

Figure 1. Quasistatic models of the potential along the field line inferred from the observations. The solid curves represent equipotential surfaces.

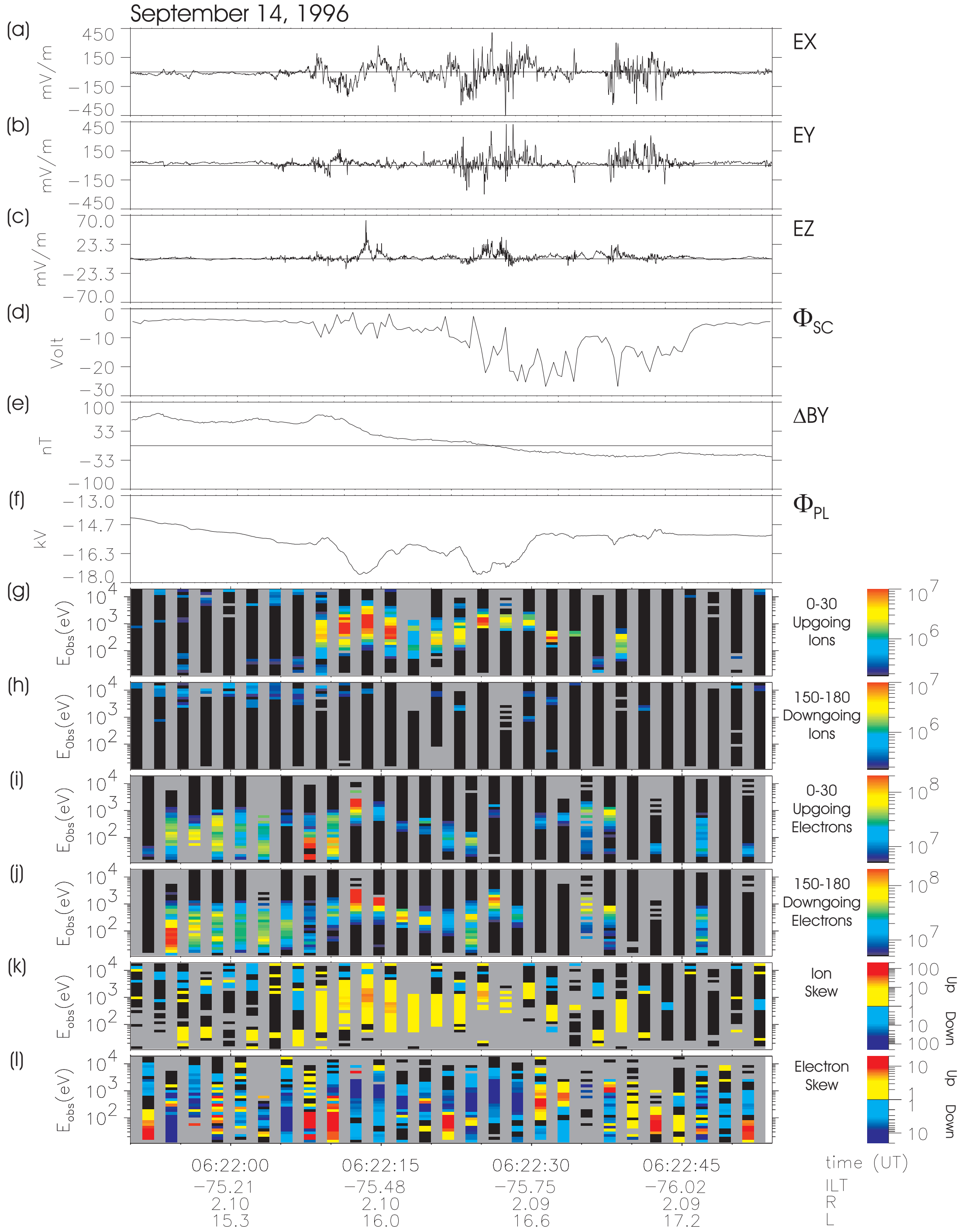

Plate 1. A southern auroral zone crossing near local noon on September 14, 1996. Shown are (a)-(c) the components of the electric field vector in field-aligned coordinates, (d) the spacecraft potential, (e) the east-west perturbation magnetic field, (f) the plasma potential, (g)-(h) spectrograms of the field-aligned and field-opposed differential ion energy flux, respectively, (i)-(j) spectrograms of the field-aligned and field-opposed differential electron energy flux, and spectrograms of the (k) ion skew and (l) electron skew.

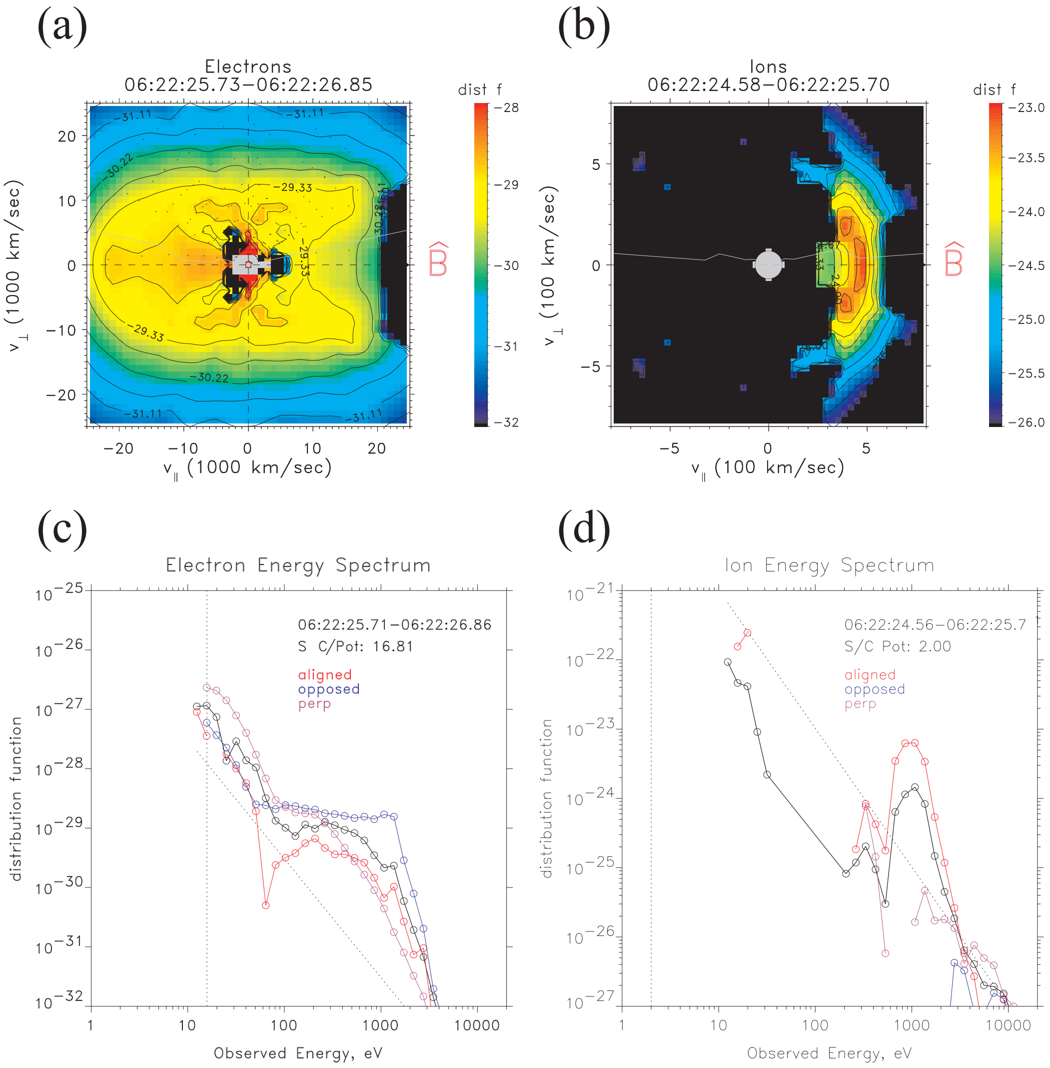

Plate 2. Electron (a) and ion (b) distribution functions in $v_{\|} - v_{\perp}$ space in the vicinity of the $E_{\|}$ event at 0622:26. Also shown are the corresponding electron (c) and ion (d) energy spectra aligned (red curve), opposed (blue curve), and perpendicular (magenta curve) to the magnetic field vector.

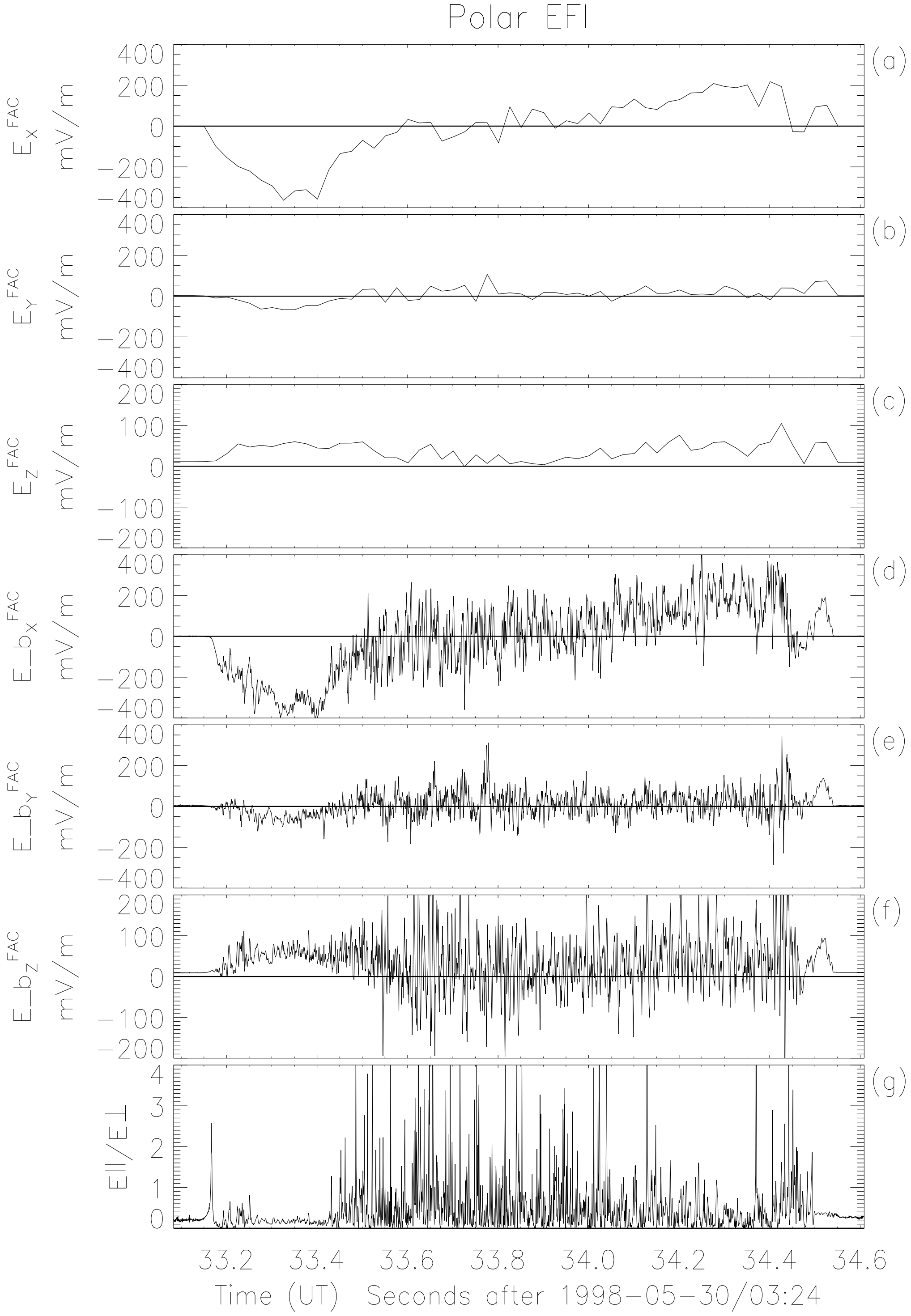

Figure 2. A southern auroral zone crossing near local midnight on May 30, 1998. Shown are (a)-(c) the components of the electric field vector in field-aligned coordinates sampled at 40 Hz, (d)-(f) the components of the electric field vector in field-aligned coordinates sampled at 1600 Hz, and (g) the ratio $E_{||}/E_{\perp}$.

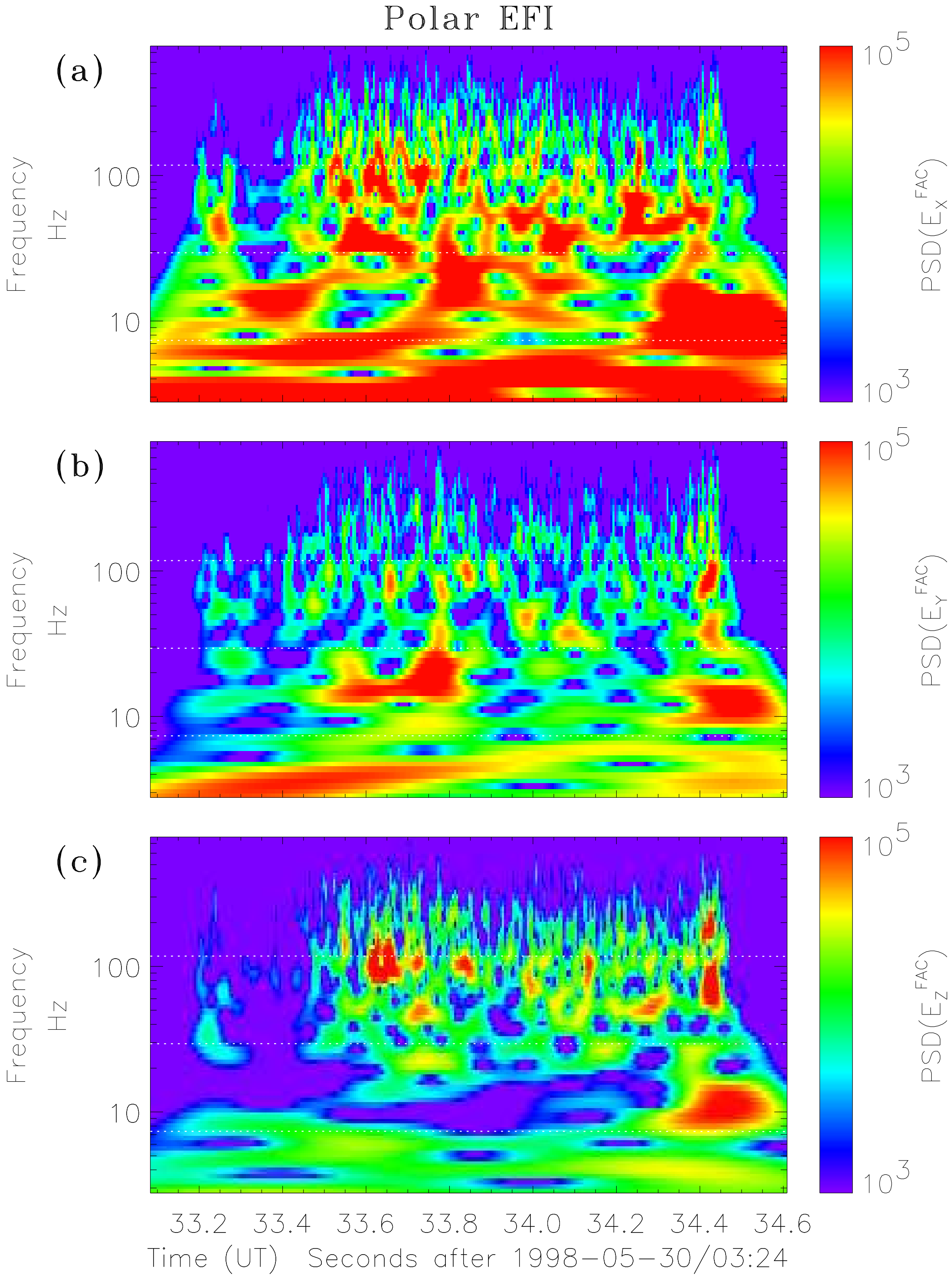

Plate 3. Time-frequency power spectra based on Morlet wavelet analysis of the three components of the burst electric field vector in field-aligned coordinates.

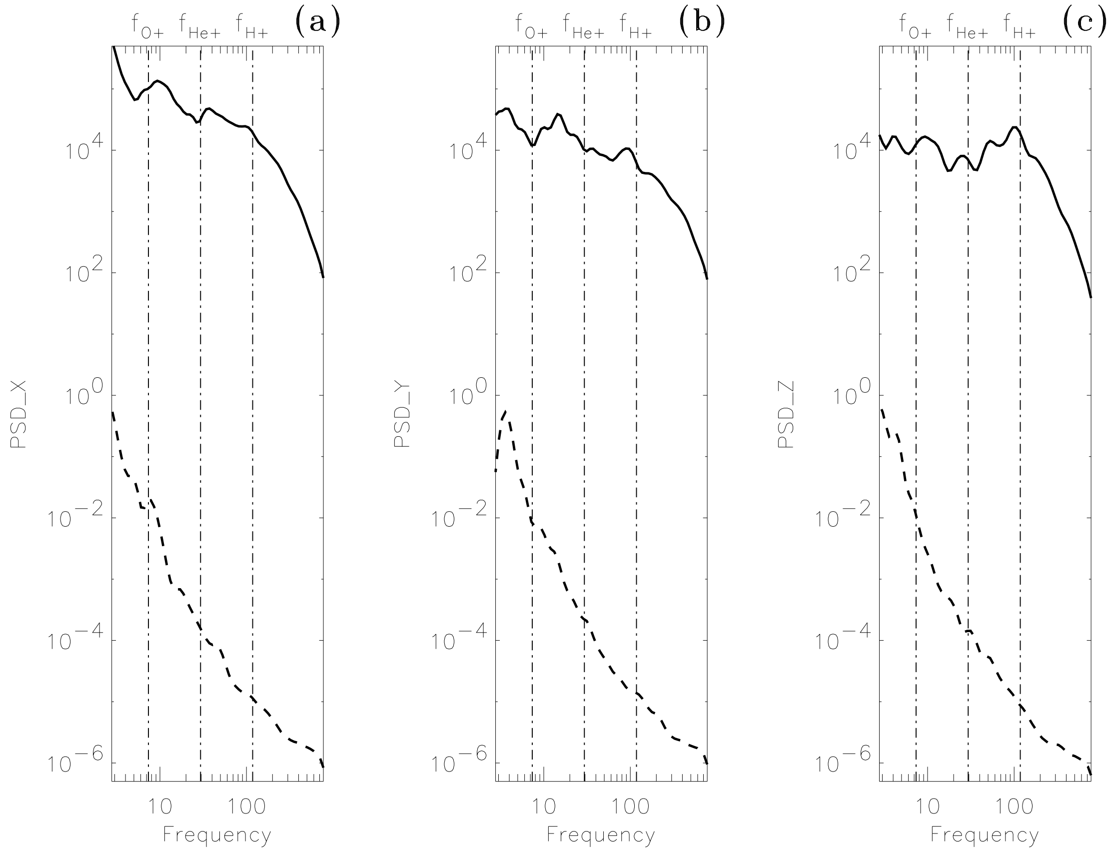

Figure 3. The power spectra of the components of the burst electric field data in the FAC system (solid curve) and corresponding search coil magnetic field power spectra (dashed curves).

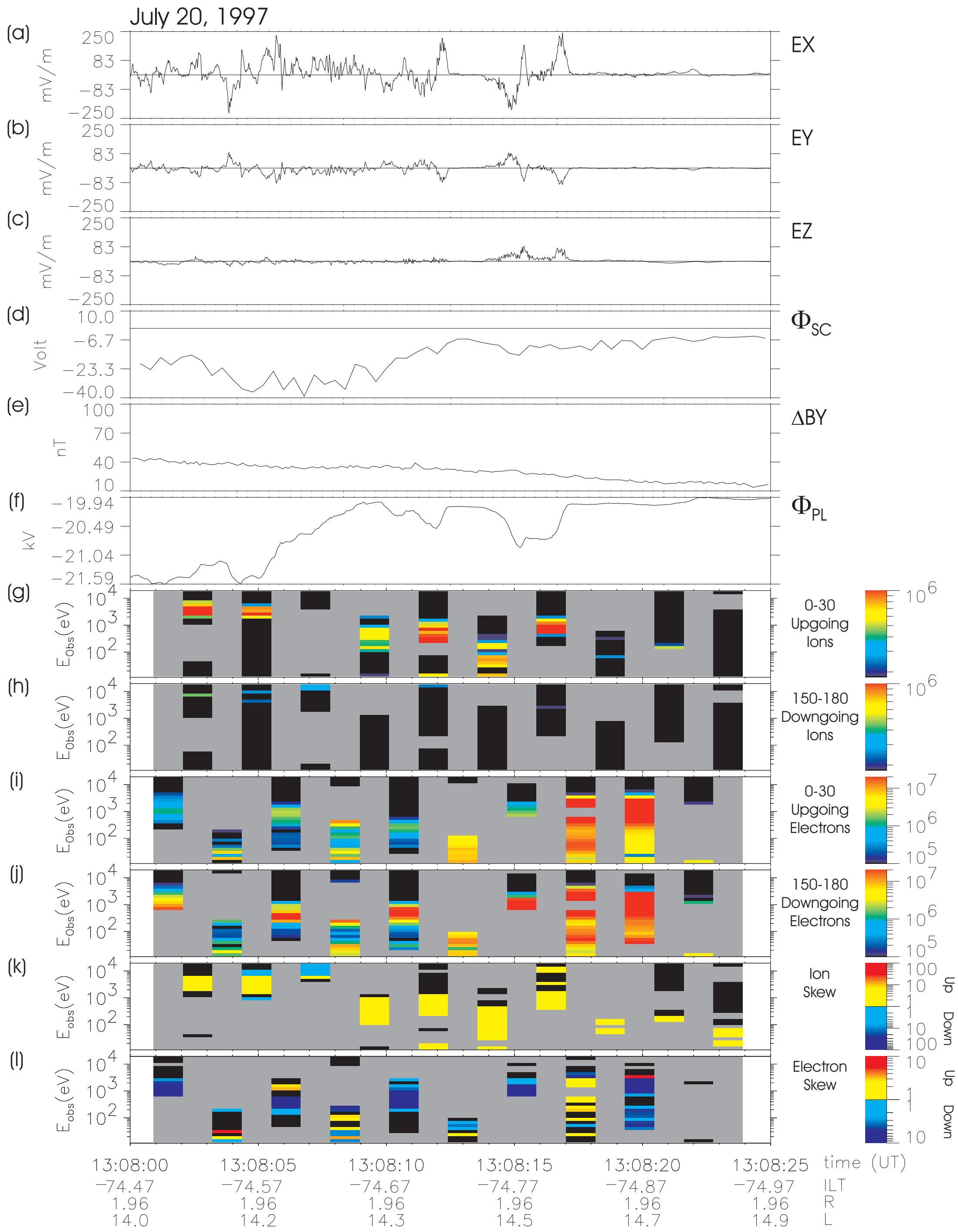

Plate 4. A southern auroral zone crossing in the evening sector on July 20, 1997. Shown are (a)-(c) the components of the electric field vector in field-aligned coordinates, (d) the spacecraft potential, (e) the east-west perturbation magnetic field, (f) the plasma potential, (g)-(h) spectrograms of field-aligned and field-opposed differential ion energy flux, respectively, (i)-(j) spectrograms of field-aligned and field-opposed differential electron energy flux, and spectrograms of the (k) ion skew and (l) electron skew.

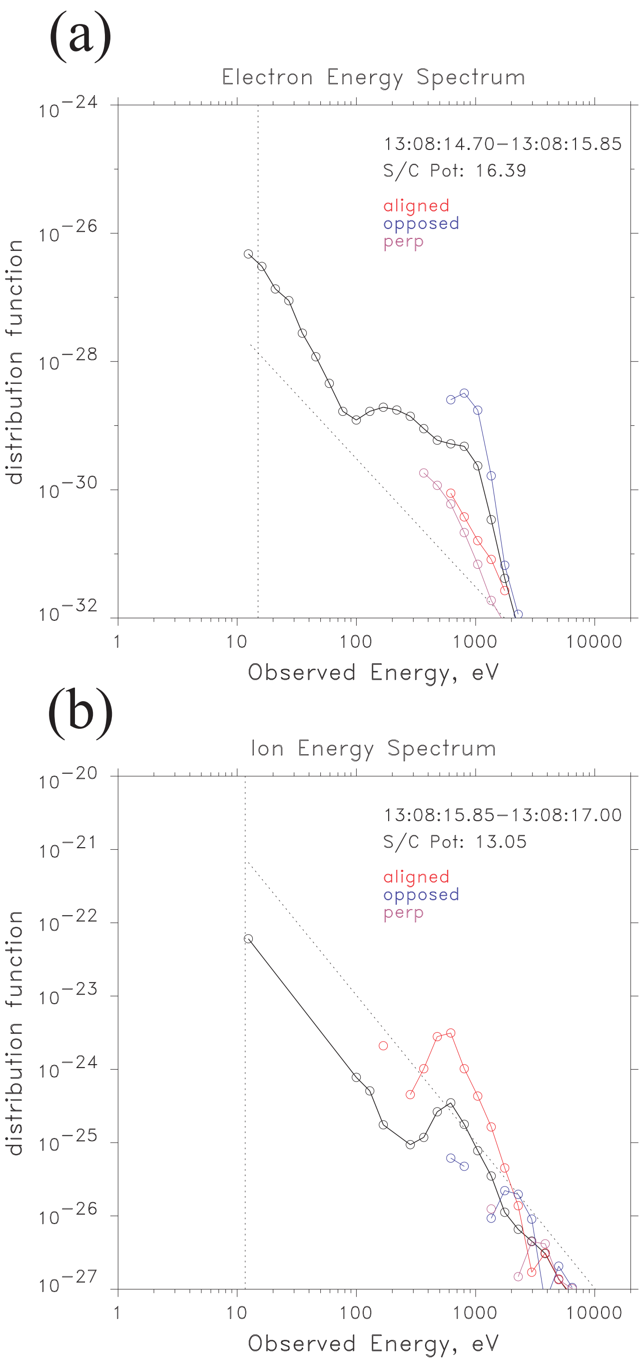

Plate 5. The (a) electron and (b) ion spectra in the vicinity of the $E_{||}$ events. The color code denotes the spectra aligned (red curve), opposed (blue curve), and perpendicular (magenta curve) to the magnetic field vector.

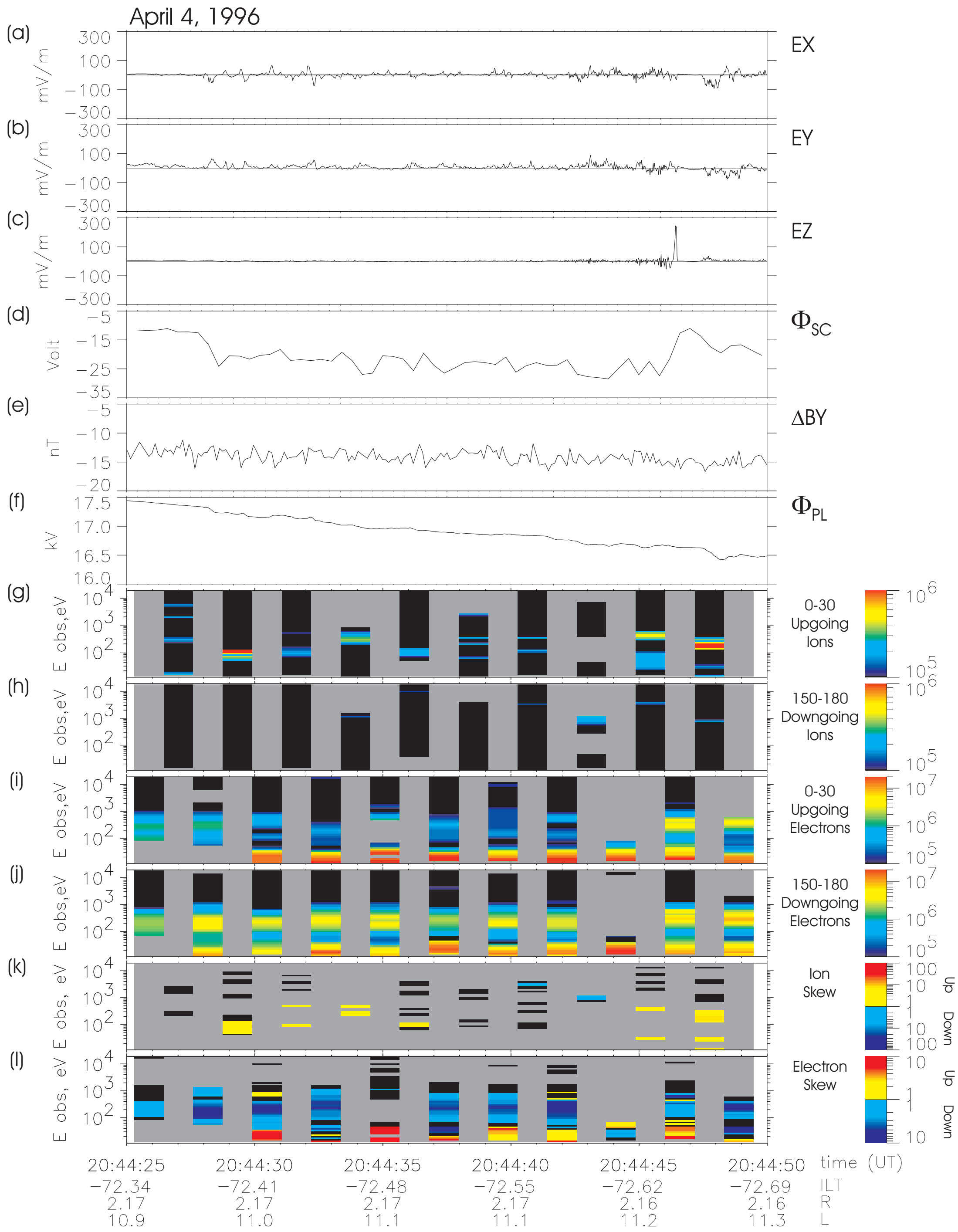

Plate 6. A southern auroral zone crossing near local midnight on April 4, 1996. Shown are (a)-(c) the components of the electric field vector in field-aligned coordinates, (d) the spacecraft potential, (e) the east-west perturbation magnetic field, (f) the plasma potential, (g)-(h) spectrograms of field-aligned and field-opposed differential ion energy flux, respectively, (i)-(j) spectrograms of field-aligned and field-opposed differential electron energy flux, and spectrograms of the (k) ion skew and (l) electron skew.

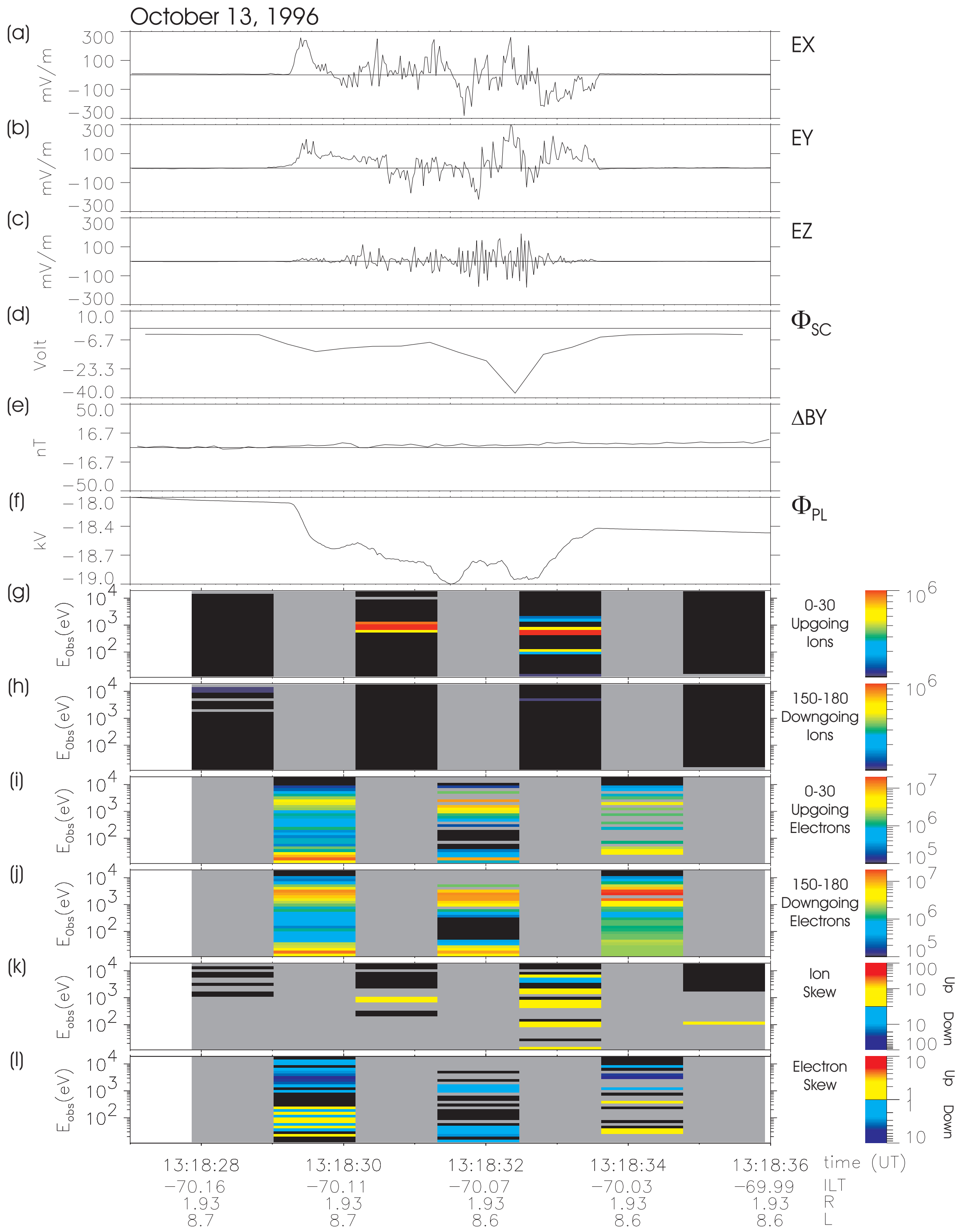

Plate 7. A southern auroral zone crossing near local midnight on October 13, 1996. Shown are (a)-(c) the components of the electric field vector in field-aligned coordinates, (d) the spacecraft potential, (e) the east-west perturbation magnetic field, (f) the plasma potential, (g)-(h) spectrograms of field-aligned and field-opposed differential ion energy flux, respectively, (i)-(j) spectrograms of field-aligned and field-opposed differential electron energy flux, and spectrograms of the (k) ion skew and (l) electron skew.

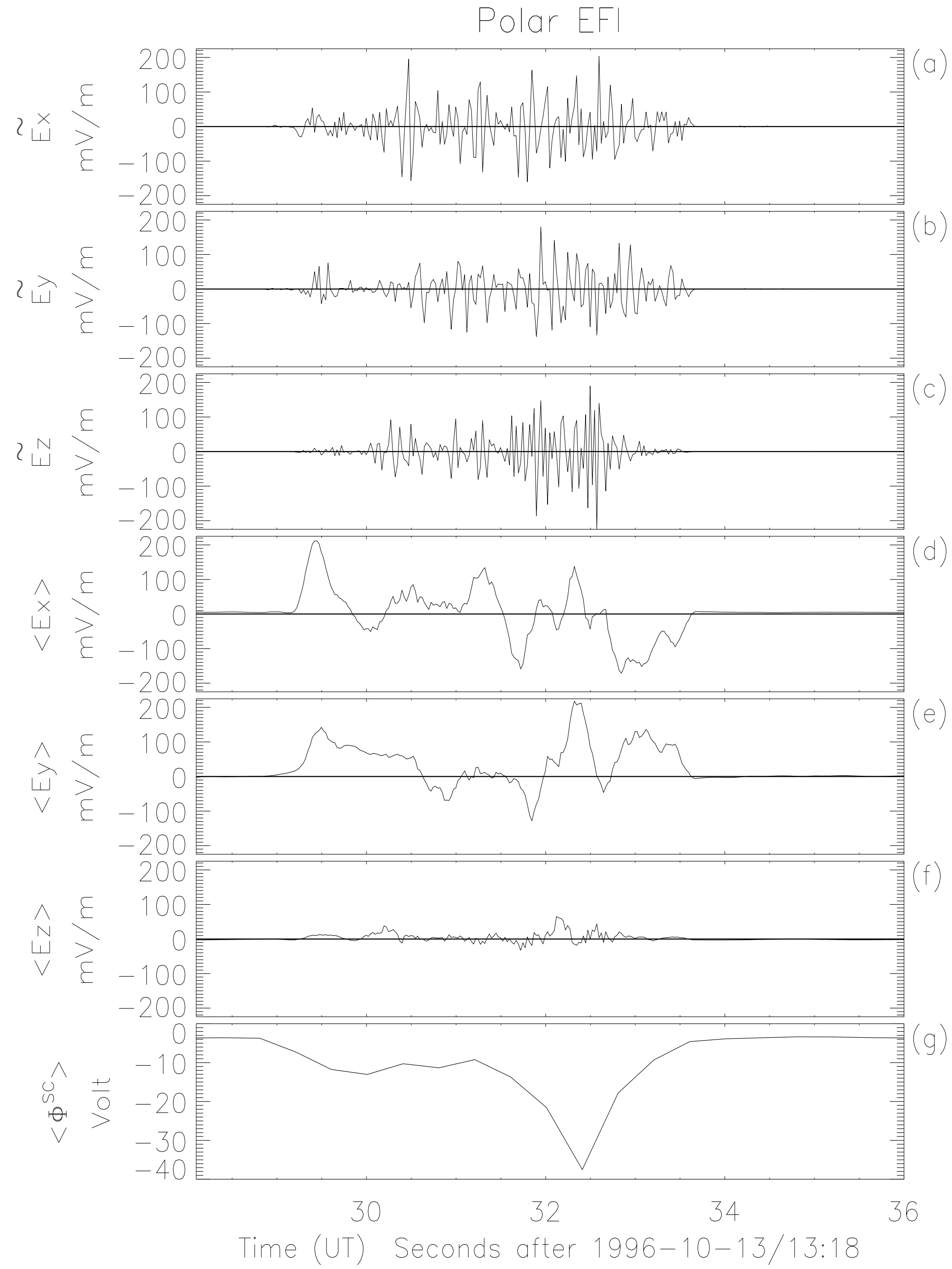

Figure 4. Depicts (a)-(c) the detrended AC components of the the electric field, (d)-(f) the boxcar averaged electric field components, and (g) the spacecraft potential.

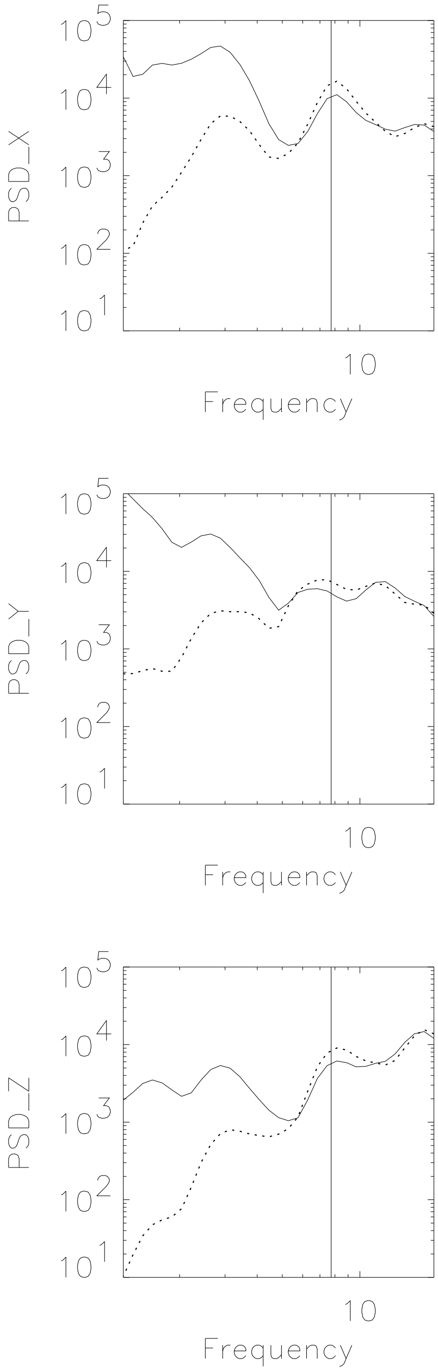

Figure 5. The power spectra of the electric field data (solid curve). Also shown are the power spectra of the detrended AC electric field components.

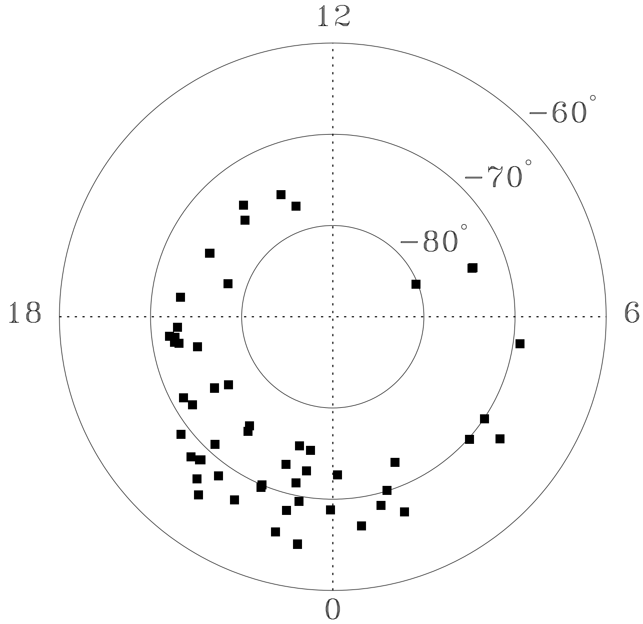

(a)

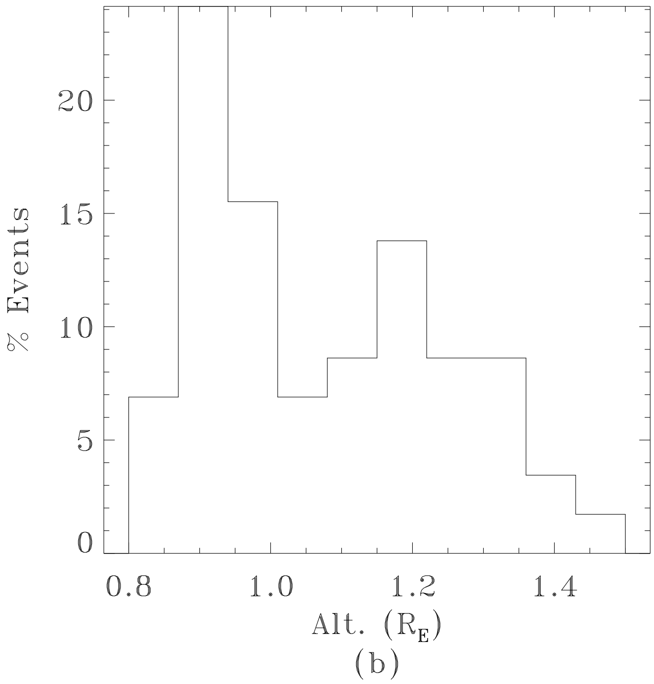

(b)

Figure 6. The geographic location of events as a function of invariant latitude and magnetic local time (a), and a histogram of the sampled parallel electric field altitudes (b).

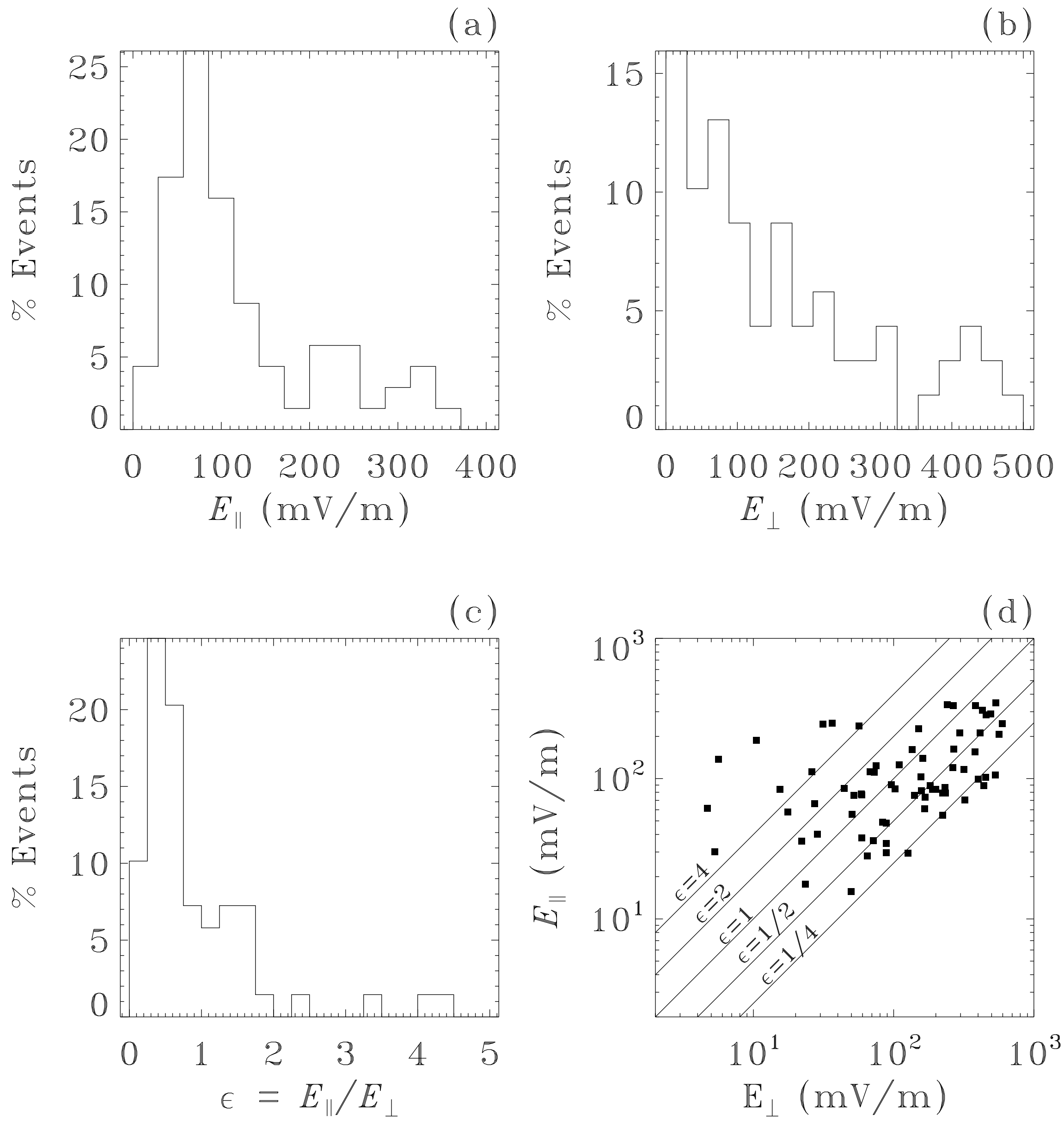

Figure 7. Histograms of (a) the magnitude of $E_{\|}$ (b) the magnitude of $E_{\perp}$, and (c) the ratio $\epsilon = E_{\|}/E_{\perp}$. Also shown (d) is a scatter plot of $E_{\|}$ and $E_{\perp}$. The solid lines represent different values of ϵ.

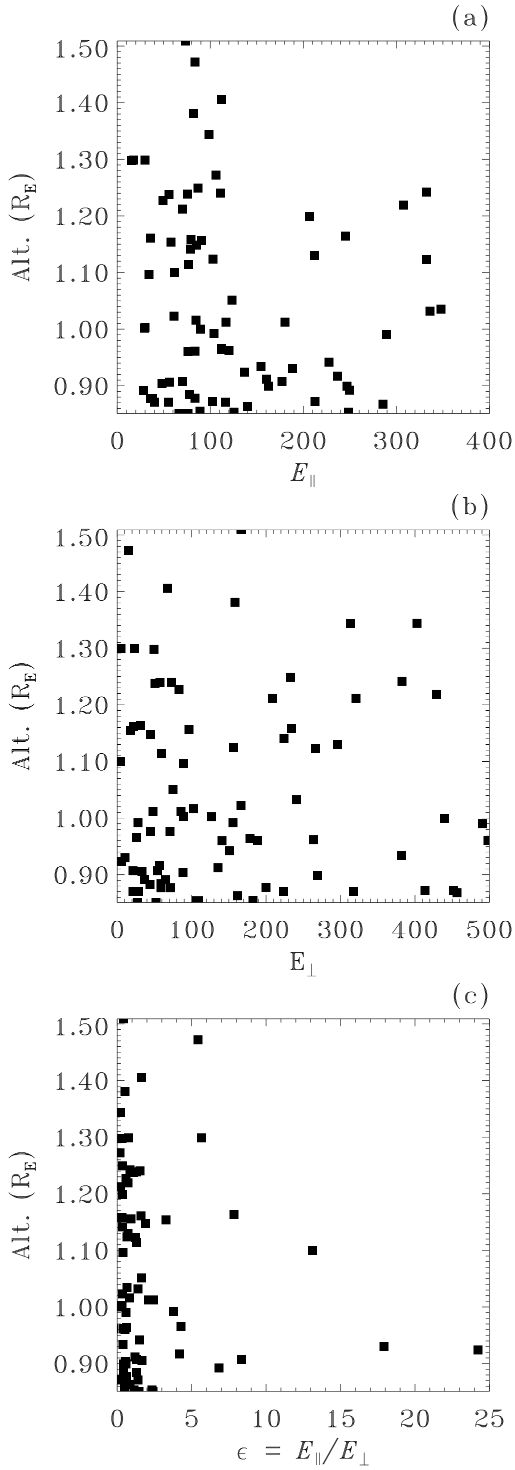

Figure 8. Observed altitude dependence of (a) $E_\parallel$ (b) $E_\perp$, and (c) $E_\parallel/E_\perp$.

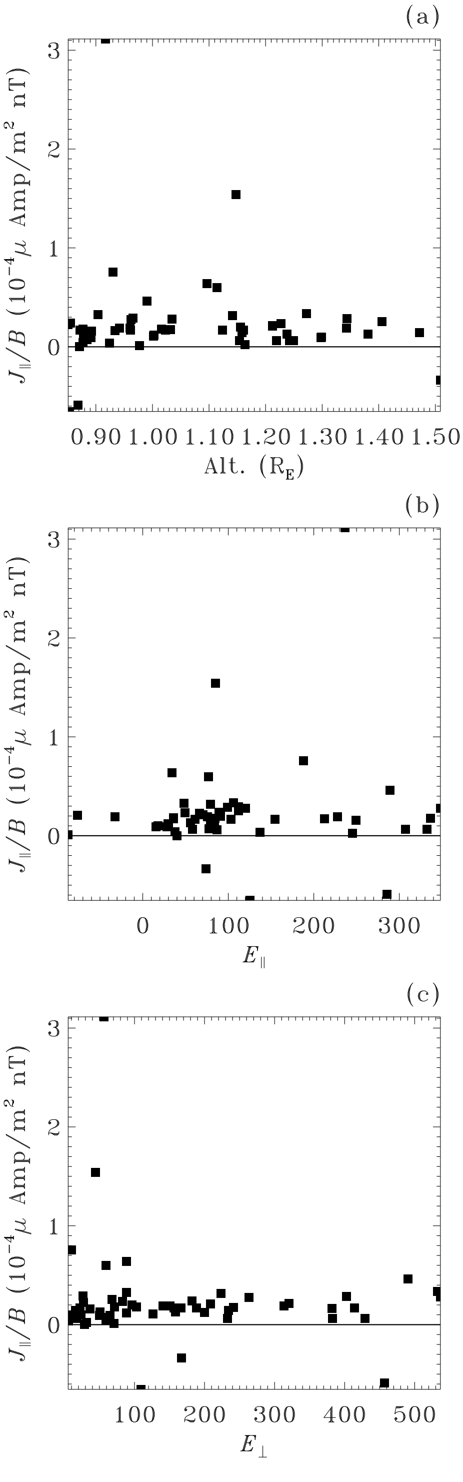

Figure 9. Comparisons of $J_{||}/B$ (a) with altitude, (b) $E_{||}$, and (c) $E_{\perp}$.

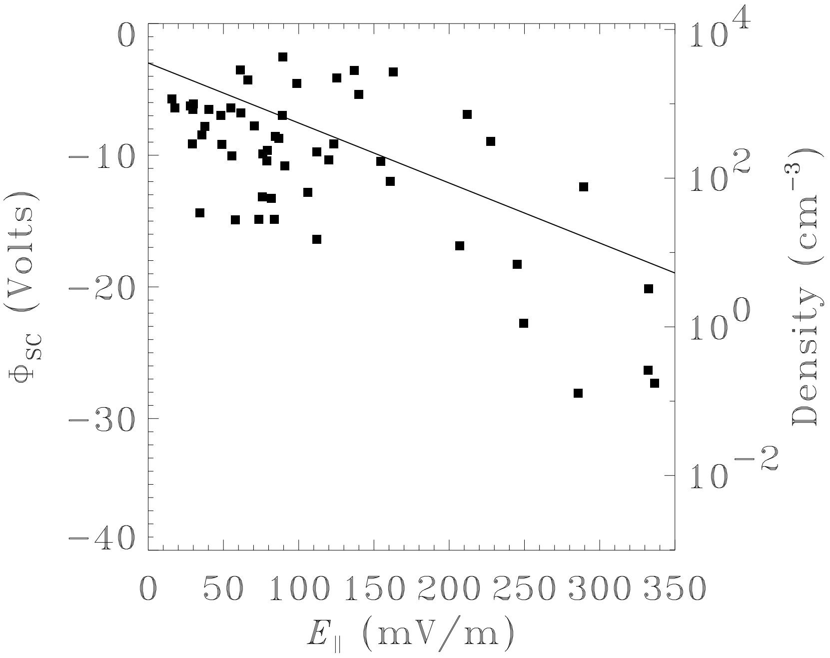

Figure 10. Comparison of the negative of the spacecraft floating potential Φ_{SC} with the measured parallel electric field $E_{||}$.

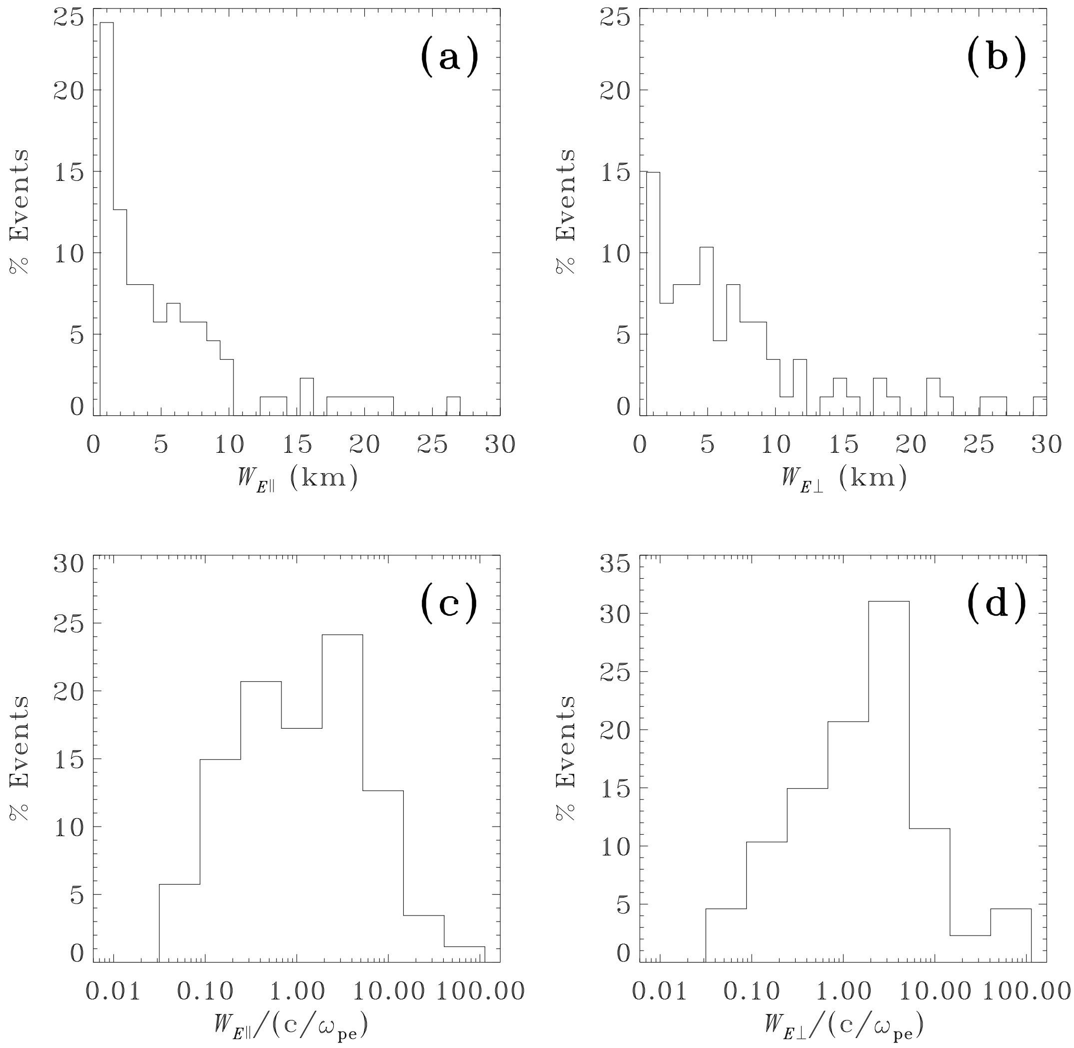

Figure 11. The distribution of the spatial widths of (a) the parallel electric field and (b) the corresponding perpendicular field structures. Also shown are the distributions of (c) $E_{\|}$ widths and (d) $E_{\perp}$ widths normalized by the electron inertial length c/ω_{pe}.

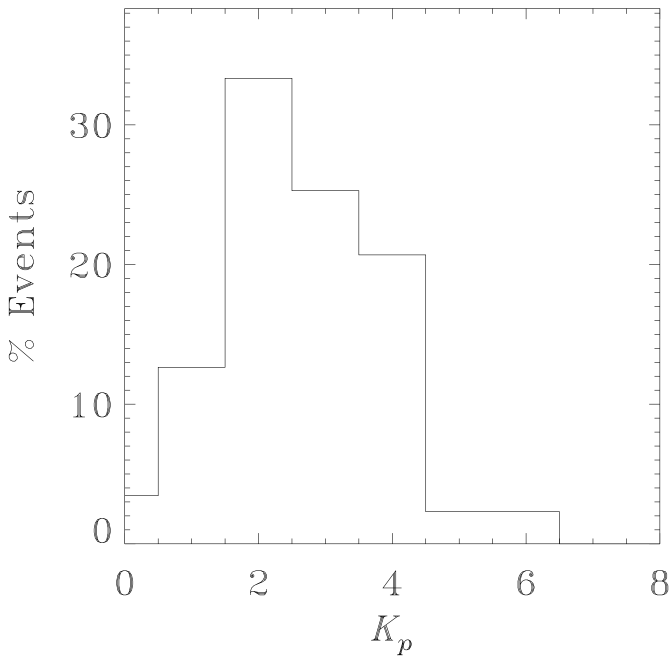

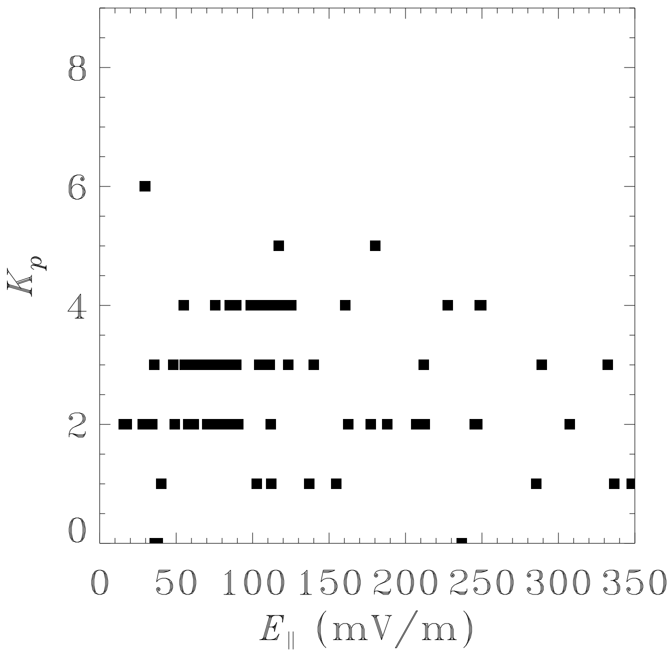

Figure 12. (a) Distribution of 3 hour averaged K_p values and (b) comparison of K_p with $E_{\|}$.